Science
AAAS

# Supplementary Materials for

## Erosion of heterogeneous rock drives diversification of Appalachian fishes

Maya F. Stokes *et al*.

Corresponding author: Maya F. Stokes, mfstokes@fsu.edu

*Science* **380**, 855 (2023)
DOI: 10.1126/science.add9791

**The PDF file includes:**

Materials and Methods
Figs. S1 to S12
Tables S1 to S6
References

**Other Supplementary Material for this manuscript includes the following:**

MDAR Reproducibility Checklist
Data S1 to S4

## Materials and Methods

Locality Data

*Nothonotus chlorobranchius* and *N. camurus* locality data were obtained from the Fishnet2 Portal (www.fishnet2.net). The presence data were supplemented with biodiversity inventory data documented across the upper Tennessee River basin by the Tennessee Valley Authority (TVA). The curated locality data are in Data S1. We leveraged the TVA inventories to derive *N. chlorobranchius* presence and absence data. To do so, we defined 7-km-long river reaches. We classified any reach containing a FishNet2 or TVA *N. chlorobranchius* observation as "present". If a reach had no *N. chlorobranchius* presence points, but did contain a TVA survey site, we classified the reach as "absent". We compared the stream gradient, predominant rock type, and median bed-sediment particle size in the presence and absence stream reaches (Fig. S1). We restricted the fish distribution analysis to upstream of the confluence of the Hiwassee River. For our topographic analyses, we used the Shuttle Radar Topography Mission (SRTM) 90-m digital elevation model (DEM) (*40*). Our analysis was conducted using the MATLAB toolkit TopoToolbox (*41*). Geologic data were acquired from the USGS State Geologic Map Compilation (*42*). To simplify the USGS state geologic maps, we classified each unit's major rock type into one of the rock type categories listed in the legend of Fig. 1. To characterize the sediment, we used the results from a machine-learning algorithm that estimated median river bed-sediment particle size across the conterminous United States (*43*). We note that channel slope and rock type are used as predictors in the machine-learning algorithm, and therefore the modeled grain size may not be independent of other variables considered here.

We augmented our analysis of fish presence and absence localities with channel survey data from a Tennessee Department of Environment and Conservation report (*44*), including

channel slope, bankfull width, depth, and cross-sectional area, and water discharge. To account for the relationship between channel geometry and water discharge when comparing stream reaches in the Blue Ridge and Valley and Ridge, we performed an analysis of covariance (ANCOVA). We used regressions of log-transformed channel geometry variables versus log-transformed water discharge (Fig. S1C) to calculate adjusted means for the two physiographic provinces. An assumption of homogeneous regression slopes (similar relationships between channel geometry and water discharge in the two physiographic regions) is met for channel slope, depth, and cross-sectional area (Tables S1-S3) but not for channel width ($F = 6.12$, $p = 0.018$). No further analysis was performed on the channel width data. When accounting for the relationship with water discharge, Blue Ridge rivers are steeper, shallower, and have smaller cross-sectional areas than Valley and Ridge rivers (Table S4). We performed a similar analysis for the channel-slope data derived from the DEM using drainage area instead of water discharge as the independent variable (Fig. S1D). This analysis also does not meet the assumption of homogeneous regression slopes ($F = 5.34$, $p = 0.021$); however, visual inspection of the regression suggests that larger streams are less steep in the Valley and Ridge than in the Blue Ridge, but that smaller streams may have similar gradients in the two regions. We found no significant linear relationship between modeled median bed-sediment particle size and drainage area, but to ensure we were comparing similarly sized rivers in the two regions, we binned the presence and absence localities by drainage area and compared the average modeled median bed-sediment particle size in rivers of comparable sizes (Fig. S1F). We used a two-tailed t-test to assess whether river reaches with or without *N. chlorobranchius* had, on average, significantly different median bed-sediment particle sizes. The median bed-sediment particle size is, on

73 average, larger in Blue Ridge rivers – a relationship that is significant ($p < 0.05$) in all drainage
74 area bins except for one (drainage area of 200 – 445 $km^2$; $p = 0.06$).
75
76 Taxon and Specimen Sampling
77 In addition to sampling 177 specimens of *Nothonotus chlorobranchius* from 39 sampling
78 locations across the species' geographic distribution in the upper Tennessee River system, we
79 sampled 286 specimens comprised of 20 recognized species of *Nothonotus.* Among the 463
80 specimens included in this study, 214 of them have previously published sequence data for the
81 mitochondrial gene *cytb (20, 29, 30, 45, 46).* Specimens collected for this study were euthanized
82 upon capture using tricaine methanesulfonate (MS-222), commonly used for sedation and
83 euthanasia of fish and amphibians, and the right-side pectoral fin was clipped to provide tissue
84 for DNA extraction. Fin-clips were stored in 100% non-denatured ethanol, and the whole-body
85 specimens were fixed in 10% formalin before being transferred to 70% ethanol for long-term
86 preservation. Fin-clips were catalogued and deposited at the Yale Fish Tissue Collection
87 (YFTC). Voucher specimens were catalogued at the Yale Peabody Museum of Natural History
88 (YPM), the North Carolina State Museum (NCSM), the Illinois Natural History Survey (INHS),
89 or the University of Tennessee (UT) fish collection (see Data S2-S3). All handling of animals
90 was carried out in accordance with protocols approved by Yale University IACUC (No. 2018-
91 10681) and appropriate collecting permits.
92
93 Double-Digest Restriction Site Associated DNA (ddRAD) Sequencing
94 We extracted genomic DNA using a Qiagen DNeasy Tissue Extraction Kit (Qiagen, Valencia,
95 CA, USA), following the manufacturer's protocols. We quantified the DNA concentrations in

each sample using a Qubit 3.0 Flourometer (Thermo Fisher Scientific, Waltham, MA, USA) and visually assessed the quality of the DNA using gel electrophoresis before proceeding. The preparation of ddRAD libraries followed protocols outlined in Peterson et al. *(47)* and as applied by Kim et al. *(48)*. Following DNA extraction and quantification, approximately 400 ng of DNA from each sample was digested using PstI/MspI restriction enzymes, ligated with 96 unique barcodes per plate, and then amplified using polymerase chain reaction (PCR). We normalized DNA concentrations across samples after ligation and PCR amplification and purified the samples using a QIAquick PCR Purification Kit (Qiagen, Valencia, CA, USA). Purified PCR products for each batch were pooled into one 96-sample library and size-selected for fragments ranging between 300 and 500 bp using a BluePippin 2% cassette (Sage Science, Beverly, MA, USA). Each size-selected library was validated using a 2100 Bioanalyzer (Agilent, Santa Clara, CA, USA), and DNA fragments were sequenced using 100 bp single-end sequencing on an Illumina Hiseq 4000 at the University of Oregon GC3F facility (http://gc3f.uoregon.edu).

The sequence data were processed using ipyrad version 0.9.68 (*49*). We employed the default settings with the following exceptions: 'denovo' for the assembly method, 'ddrad' for the datatype, 'TGCAG, CCG' for the restriction overhang, and '0.96' for the clustering threshold (*50*). The minimum number of specimens sharing a locus, hereafter referred to as 'min', was set to maintain a missing portion below 15% in each data matrix.

Mitochondrial DNA Sequencing

The complete mitochondrial cytochrome *b* (*cytb*) gene was amplified using PCR and primers GLU2 and ProR1. Amplified PCR products were purified using 20% polyethylene glycol DNA precipitation and sequenced on an Applied Biosystems 3730xL (Applied Biosystems, Foster

City, CA, USA) at the Yale Keck DNA Sequencing Facility. Sequences were trimmed and assembled using Geneious v.8.0.5 (http://www.geneious.com), aligned using MAFFT version 7.409 (*51*), and then translated into amino acids using MEGA version 6.0 (*52*) to verify gene regions and check for premature stop codons. We supplemented the data sequenced in this study with those from previously published datasets (*20, 29, 45, 46*). The original publication and GenBank Accession (*53*) numbers for each sequenced individual can be found in Data S2.

Phylogenetic Analysis

We used a maximum-likelihood approach for phylogenetic inference using the software IQ-TREE v.2 (*54*). We inferred phylogenies from four phylogenetic datasets. First, we used the ddRAD sequence data to assess the phylogenetic placement and monophyly of *Nothonotus chlorobranchius* within *Nothonotus* (Fig. S2). Second, we assessed mitochondrial introgression among species of *Nothonotus* using *cytb* sequence data (Fig. S5). The third and fourth analyses were aimed at relationships within *N. chlorobranchius* based on separate analyses of the ddRAD (Fig. 2A) and mtDNA *cytb* (Fig. 2B) datasets. For all analyses, the best-fit sequence substitution model was determined using ModelFinder (*55*) implemented in IQ-TREE on the basis of the Bayesian information criterion (BIC). We assessed topological support with 1,000 ultrafast bootstrap replications (*56*).

The *Nothonotus* ddRAD phylogeny was inferred using a dataset of 39,715 ddRAD loci sampled from 27 selected specimens of *Nothonotus chlorobranchius* from geographically spaced sampling locations and 136 specimens of 18 other species of *Nothonotus* (Fig. S2; Data S2). The minimum number of specimens required to share a locus was set to 118 (min=118) during the ipyrad filtering, and the TVM+F+R2 substitution model was selected. We then inferred an

mtDNA gene tree inferred for 15 species of *Nothonotus* (Fig. S5), including 156 specimens of *N. chlorobranchius* and 155 outgroup taxa, including 114 specimens of *N. rufilineatus,* a species that has previously been observed to hybridize with multiple species of *Nothonotus (29).* The TIM3+F+I+G4 substitution model was selected for this analysis. We rooted both the ddRAD phylogeny and mtDNA gene tree for *Nothonotus* with *N. juliae*, following its phylogenetic resolution in previous phylogenetic analyses of darters (Etheostomatinae) (*20, 30*). The resulting trees, as well as previous darter phylogenies (*20, 30*), resolve the lineage consisting of *N. bellus* and *N. camurus* as a sister lineage of *N. chlorobranchius* (Fig. S2, Fig. S5).

We analyzed the relationships within the *Nothonotus chlorobranchius* complex using both the ddRAD (Fig. 2A) and the mtDNA *cytb* (Fig. 2B) datasets. We included *N. bellus* and *N. camurus* as outgroup taxa. The ddRAD dataset comprised 15,210 loci sequenced from 141 specimens of *N. chlorobranchius,* two specimens of *N. bellus*, and five specimens of *N. camurus* (min=126). The *cytb* dataset included 156 specimens of *N. chlorobranchius*, two specimens of *N. bellus* and three specimens of *N. camurus.* The TVM+F+R2 and TN+F+G4 models were identified as the best-fit sequence substitution models for the ddRAD and *cytb* datasets, respectively.

Divergence Time Estimation

To calibrate our estimate for the timing of divergence between lineages of *Nothonotus chlorobranchius,* we first estimated a rate of nucleotide substitution in a concatenated dataset consisting of 7,339 concatenated ddRAD loci (totaling 629,563 base pairs) sampled from a single specimen from 18 species of *Nothonotus* (Data S2; Fig. S10A). We deployed two calibration points inferred from a previously published multispecies coalescent species-tree

analysis of 92 percid species using 12 Sanger-sequenced nuclear loci (*30*). The first calibration is the age of the most recent common ancestor (MRCA) of *N. juliae* and all other species of *Nothonotus* [mean, 19.38 Ma; 95% highest posterior density (HPD), 22.40–16.32 Ma]. The second calibration is the MRCA of the clade that includes all species of *Nothonotus* excluding *N. juliae* (mean, 13.64 Ma; 95% HPD, 16.41–11.00 Ma). We used these two calibration points as priors in BEAST (*57*) v. 2.6.3 assuming a normal distribution over the range of the upper and lower bounds of the inferred HPDs. For all BEAST analyses, we used a Birth-Death tree prior, the uncorrelated lognormal relaxed clock model (ucld), and a mean of 10.0 for the "ucld.mean" parameter with an exponential distribution. Two independent runs of one hundred million generations were performed, sampling parameters and trees every 10,000 generations.

Next, we used the estimated rate of nucleotide substitution of the ddRAD loci in *Nothonotus* ($3.89 \times 10^{-4}$ substitutions per site per million years) as a prior in a BEAST analysis to estimate the age of the MRCA of *N. bellus, N. camurus,* and *N. chlorobranchius.* For this analysis, we used a ddRAD dataset that included 24,247 loci (2,126,476 base pairs) sampled from a single specimen from each lineage of *N. chlorobranchius* resolved in our more inclusive phylogenetic analyses (Fig. S10B; Data S2). A single specimen of each *N. bellus* and *N. camurus* were included as outgroups. We use the resulting tree as our first of two estimates for the timing of the Little Tennessee, the earliest-diverging clade (Fig. S10).

For our second estimate of the divergence times of the major lineages of *Nothonotus chlorobranchius*, we used the multispecies coalescent framework as implemented in the SNAPP module (*58*) in BEAST. We treated each of the eight major lineages of *N. chlorobranchius* as species and subsampled three specimens for each of these species and *N. camurus.* Using the R package "phrynomics" (http://github.com/bbanbury/phrynomics), the dataset was reduced to

include 2,237 biallelic and unlinked SNPs that were shared by all specimens in the SNAPP analyses. We estimated divergence times among lineages of *N. chlorobranchius* using a strict molecular clock method in SNAPP. The phylogeny inferred from the SNAPP species tree analysis was used as the starting tree in the molecular clock analysis, and the taxon sampling was identical to that used in the SNAPP species tree analysis. The age of the MRCA of *N. camurus* and *N. chlorobranchius*, inferred from the BEAST divergence time analysis using the nucleotide substitution rate (mean 8.06 Ma; 95% HPD 10.28–6.47 Ma), was treated as the calibration point. Two independent runs of twenty million generations were performed, sampling parameters every 200 generations. For all BEAST and SNAPP analyses, Tracer v.1.7 was used to check stationarity, to determine the number of generations discarded as burn-in, and to confirm that effective sample sizes (ESS) were over 200. The converged runs were combined with LogCombiner (https://www.beast2.org/programs/). Post-burnin tree samples were annotated for mean height using TreeAnnotator (https://www.beast2.org/programs), and the final trees were visualized in FigTree v.1.3.1 (http://tree.bio.ed.ac.uk/software/figtree).

Population Genomics and Species Delimitation

We calculated a population-genetics metric, the fixation index ($F_{ST}$), between 13 geographic clusters of localities across the upper Tennessee River basin to assess the degree of genetic differentiation within and between Blue Ridge tributaries. We assigned each of the 142 individuals in the ddRAD sequence data to a geographic cluster to compare within- and between-tributary differentiation (Fig. S3A). We calculated $F_{ST}$ using the R package HIERFSTAT (*60)* using the equations from Weir and Cockerham (*59*) using the ".vcf" output file from ipyrad.

We then used the concatenated ddRAD loci dataset to calculate the absolute genetic divergence ($D_{CH}$) of *N. chlorobranchius* between 23 localities, using the R package HIERFSTAT (*60*). Each locality was treated as a population. We used 63 specimens for this analysis (min=49; 51,086 loci; ~15.5% missing portion in sequence matrix). We then compared the pairwise genetic divergence to the streamwise distance between localities (Fig. S3B). We differentiated between localities within the same major tributary versus localities that are in different tributaries and thus separated by the sedimentary rocks of the Valley and Ridge. We performed a least-squares linear regression between streamwise and genetic divergence for the between-tributary comparisons and within-tributary comparisons. For each regression, we used an F-Test to determine whether the slope was significantly different than a constant model.

We also tested hypotheses of species delimitation using the genealogical divergence index (*gdi*) (*25*) for the seven major lineages of *Nothonotus chlorobranchius,* including the two located in the Little Tennessee River (mainstem and Cheoah rivers) and one in each of the Holston, Watauga, Pigeon, Nolichucky, and French Broad rivers (Fig. S3C). We included five specimens from each of the seven lineages using loci that are shared by all 35 specimens (2,672 loci). We first used the R package PopGenome (*61*) to estimate average nucleotide diversity within and between lineages (*62*). We used these estimates as priors for estimating the effective population size ($\theta$) and coalescent time ($\tau$) using the algorithm A00 of the program BPP v.4.1 (*63*). The phylogenomic relationships inferred from the IQ-TREE analysis were used as the guide species tree. We performed ten independent runs each for 150,000 generations, sampling parameters every 50 generations, with a burn-in of 50,000 generations. Tracer was used to check stationarity and to confirm that the effective sample size (ESS) was over 200.

233 Morphological Traits

234 Morphological traits were examined for 400 specimens of *Nothonotus chlorobranchius* and 30
235 specimens each of *N. camurus* and *N. bellus*. The nine traits examined included the snout length
236 and the number of the following quantities: lateral line scales, scales above the lateral line,
237 transverse scales, circumpeduncle scales, first dorsal fin (D1) spines, second dorsal fin (D2) rays,
238 anal fin rays, and pectoral fin rays. We employed principal component analysis on the nine
239 measurements (Fig. S6) and then created a fitted discriminant model using the "fitcdiscr"
240 function in MATLAB using all the data. Because of highly variable sample size among lineages,
241 we used a uniform prior probability for each class equal to $1/K$, where $K$ is the number of classes
242 (lineages). We then used the trained model to predict the lineage of each specimen. We report the
243 proportion of individuals correctly identified using the discriminant model in Fig. S6B. The raw
244 morphological trait data can be found in Data S3.

245

246 Geologic Model of Isolation

247 We reconstructed the predicted history of isolation between tributaries for planar rock contacts
248 with different attitudes. To do so, we made several simplifying assumptions. First, we assumed
249 that the river network has remained in the same location that it occupies today throughout the
250 period of study. Second, we assumed that the contact between the Blue Ridge metamorphic rocks
251 and Valley and Ridge sedimentary rocks is a dipping plane that can be characterized by a single
252 strike ($\theta$) and dip ($\alpha$). We related the strike and dip to the normal vector to the plane ($\vec{n} =$
253 $\langle a, b, c \rangle$) as

$$a = \sin\alpha \sin\theta \,, \tag{1}$$

$$b = -\sin\alpha \cos\theta \,, \tag{2}$$

$$c = -\cos\alpha\,. \quad (3)$$

We then solved for the scalar equation of a plane using the horizontal position ($x,y$) and elevation ($z$) of the surface trace of the Blue Ridge Thrust Fault,

$$ax + by + cz = d\,, \quad (4)$$

where $d$ is a constant. We relied on USGS geologic maps to locate the position of the Blue Ridge Thrust Fault in the landscape today. What we refer to as the Blue Ridge Thrust Fault comprises several local features: the Meadow Creek Fault, the English Mountain Fault, the Holston Mountain Fault, and the Great Smoky Fault (Fig. S7). These faults generally separate Ordovician and younger rocks (Valley and Ridge) from Cambrian and older rocks (the metamorphic rocks of the Blue Ridge). We extracted polylines from the USGS State Geologic Map Compilation (*42*) that correspond to these faults in local geologic maps (*64-67*). We then merged the polylines into one regional feature we refer to as the Blue Ridge Thrust Fault. All geographic data were projected in UTM Zone 17N.

For a given geometry, we assumed that any topography above the plane of the Blue Ridge Thrust Fault is composed of metamorphic rock and is, therefore, suitable *Nothonotus chlorobranchius* habitat. Conversely, we assumed that any location in the landscape with an elevation below the plane is in sedimentary rock and is not suitable habitat. Prior to constructing hypothetical phylogenies, we identified the fault geometry that best fits the present-day topography and exposure of rock using two approaches. First, we performed a least-squares fit of a plane to the surface trace of the fault, which produced the following values: $a = 4.40 \times 10^{-4}$, $b = 3.98 \times 10^{-3}$, $c = -1$, and $d = 1.52 \times 10^{4}$, corresponding to a dip angle $\alpha = 0.2°$ and a strike direction $\theta = 6.3°$ north of east (equivalently, a dip direction of 83.7° south of east). Note that dip directions (not strikes) are plotted in Figures 4 and S8. Second, we solved Equations 1 – 4 for a

given strike ($\theta$) and dip angle ($\alpha$) using the mean value of the surface trace of the fault, $x$ = 304,906 m, $y$ = 3,980,489 m, and $z$ = 510 m. We calculated the mean fraction of the landscape for which a geologic contact with a given dip direction correctly predicts the presence of either metamorphic or sedimentary rock exposed at the surface for dip angles ranging from horizontal to 20°. A dip direction ~60° south of east produces the best prediction of rock type across the upper Tennessee River basin.

We used the fault geometries to build hypothetical phylogenies varying the strike ($\theta$) and keeping the dip angle ($\alpha$) constant. Different values of $\alpha$ produce similar patterns (Fig. S9). The results presented in the main text (Fig. 4) and Fig. S8 are for $\alpha$ = 1°. We identified the farthest downstream recorded instance of *Nothonotus chlorobranchius* within each tributary (Fig. S7). We then found the total thickness of rock that would need to be added back to the landscape in order for the pathway between any two tributaries to be located entirely in metamorphic rock. We assumed that the total thickness of rock (and thus time) required to connect two populations should correlate with how distantly related the populations are. The process is visualized in Fig. 3 and Fig. S7. We note that these reconstructions assume a simplified geometry involving only two major geologic units, the Blue Ridge and Valley and Ridge, and therefore do not capture geological structures beyond the geographic extent of these two provinces. In particular, the reconstructions predict that Blue Ridge metamorphic rocks were previously exposed in the westernmost tributaries of the upper Tennessee River basin where the rocks of the Cumberland Plateau are currently exposed, but it is unlikely that the Blue Ridge thrust sheet extended that far west. This simplification does not affect our analysis substantially because the tributaries inhabited by *N. chlorobranchius* and the paths between them are in the central and eastern parts of the upper Tennessee basin. Despite their simplicity, these reconstructions are useful for

298 examining how habitat connectivity near the contact between the Valley and Ridge and Blue
299 Ridge provinces changed over time.

300 We placed pairwise comparisons of the amount of time required for a connection
301 between *Nothonotus chlorobranchius* populations into a distance matrix to construct hypothetical
302 dendrograms representing the timing of isolation between each tributary for each of the fault
303 geometries using MATLAB's "phytree" function. We compared the topology of the
304 dendrograms predicted by the geologic scenarios to dendrograms representing the history of
305 isolation inferred from the ddRAD sequence and mtDNA data (Fig. 4B,C). We excluded the
306 Hiwassee River when comparing the geologic model to the ddRAD data because the specimen
307 sampled from the Hiwassee was resolved as *N. camurus*. It was included when analyzing the
308 mtDNA gene tree because it contains *N. chlorobranchius*-like mtDNA (see main text for more
309 details). We note that specimens from the Little Pigeon and Pigeon Rivers are not monophyletic
310 in the ddRAD and mtDNA phylogenies, respectively. Therefore, we repeated the analysis
311 without these tributaries, which leads to a NE dip (as opposed to a NE or SE dip) being favored
312 in the comparison to the ddRAD dataset (Fig. S8).

313 We quantified the similarity between the dendrograms inferred from the geologic and
314 phylogenetic analyses using the R package "TreeDist". We calculated the mutual clustering
315 information, an information-theoretical metric for assessing the shared information between the
316 two trees (*68*). For this analysis, we only considered differences in the tree topologies, not
317 differences in the relative timing or distance between nodes. We normalized the values by
318 dividing the mutual clustering information value for a comparison between the geologic model
319 and dendrograms inferred from the phylogenies by the mean value for a comparison of the
320 geologic model to 1000 random dendrograms with the same number of tips.

Geologic Prediction for Absolute Timing of Isolation

Vertical river incision can be directly related to time by assuming a steady and uniform erosion rate throughout the basin. We estimated the timing of isolation of the Little Tennessee River by finding the total amount of rock needed to be added back to the landscape in order for the Little Tennessee and Watauga Rivers to be connected (Fig. S7). We then divided this value by an erosion rate to calculate how long ago the populations would have been connected by a pathway that was 100% or 50% metamorphic rock (Fig. S7). Erosion rates were estimated by measuring the concentration of the cosmogenic nuclide $^{10}$Be in stream sediment throughout the Tennessee River basin. To ensure that the simple geometric reconstruction described above is a reasonable way to estimate the timing of isolation, we additionally used a 1D numerical simulation of the topographic evolution of a river incising into different rock types to perform a similar calculation synthetically.

*Cosmogenic nuclide-derived erosion rates*

To constrain the rate at which the landscape is lowering, we measured cosmogenic-nuclide-derived basin-averaged erosion rates throughout the Tennessee River basin. We collected stream sediment from across the basin and then isolated quartz and extracted *in situ*-produced $^{10}$Be at the University of Massachusetts - Amherst Cosmogenic Nuclide Laboratory. Erosion rate data produced for this study are reported in Table S5.

We first sieved the sediment to a grain size between 250 and 850 μm and isolated quartz. Quartz was treated with hot hydrochloric acid and then purified by repeated etching in a 1 L solution of 2% hydrofluoric acid (*69*) in a heated ultrasonic bath. Heavy liquid was used to

separate dense minerals from quartz prior to the final etching. The pure quartz separates were dissolved following the addition of ~250 μg of low-level $^{9}$Be carrier. Beryllium was separated via ion chromatography following Ditchburn and Whitehead (*70*) and Stone *(71)*. The $^{10}$Be/$^{9}$Be ratios were measured via accelerator mass spectrometry at the Purdue Rare Isotope Measurement (PRIME) Laboratory and normalized to the 07KNSTD standard (*72*). We ran two process blanks (with $^{10}$Be/$^{9}$Be ratios: $3.85(\pm3.03) \times 10^{-16}$; $4.07(\pm3.20) \times 10^{-16}$) and subtracted the average $^{10}$Be/$^{9}$Be ratio of the process blanks from the sample measurements. We propagated the analytical uncertainty associated with each sample measurement and the mean blank uncertainty to represent 1σ analytical uncertainty on each of the measurements. We then used the Balco et al. (*73*) calculator to derive erosion rates from the measured $^{10}$Be/$^{9}$Be ratios. We used LSDtopotools to calculate an effective latitude, longitude, and atmospheric pressure in each basin (*74*). We assumed that there is no topographic shielding (*75*) and that the density of the material is 2.65 g cm$^{-3}$. We used the Lal/Stone cosmogenic nuclide production scaling (*76, 77*) and report the external uncertainty in erosion rates. The inputs to the Balco et al. (*73*) calculator are in Table S6.

We supplemented the erosion rates collected in this study with a compilation of previously published measurements throughout the central and southern Appalachian Mountains (*78-84*). The compilation is available in Data S4.

*Numerical simulation of river incision*

We simulated the evolution of the longitudinal profile of the Nolichucky River with the widely used stream-power equation (*85*), which predicts the evolution of the land surface elevation ($z$)

365 through time ($t$) and upstream distance ($x$) as a function of an uplift rate ($U$), an erodibility
366 constant ($K$), drainage area ($A$), slope ($\partial z/\partial x$), and two exponents ($m$ and $n$),

$$\frac{\partial z}{\partial t} = U - K(x)A(x)^m \left|\frac{\partial z}{\partial x}\right|^n . \quad (5)$$

367 The steady-state profile of a channel can be determined by setting $\partial z/\partial t = 0$ and integrating Eq. 5
368 with respect to $x$, yielding

$$z(x) = z_b + \left(\frac{U}{KA_0^m}\right)^{\frac{1}{n}} \chi , \quad (6)$$

369 where $A_0$ is a reference drainage area used to scale the value of $\chi$,

$$\chi = \int_{x_b}^{x} \left(\frac{A_0}{A(x')}\right)^{\frac{m}{n}} dx' , \quad (7)$$

370 and the subscript $b$ refers to a base-level location (*86*). The erodibility coefficient, $K$, can be
371 estimated with a χ-transformed river profile: the slope of a plot of $z$ against χ is equivalent to the
372 normalized steepness index, $k_{sn}$ (*86, 87*), which can be related to the erodibility coefficient $K$,

$$K = \frac{E}{k_{sn}^n} , \quad (8)$$

373 where $E$ is the erosion rate, which in a steady-state river profile is equal to the uplift rate $U$, or
374 equivalently a rate of base-level fall $B$. To estimate the erodibility coefficient $K$ for metamorphic
375 rock, we regressed elevation ($z$) versus χ for the Nolichucky River upstream of the contact
376 between sedimentary and metamorphic rock. We used an iterative process to select the value of
377 $m/n$ that minimized the least-squares residual of the χ-transformed profile. We then solved for $K$
378 using Eq. 8; we used values of $n$ equal to 1 and 1.5, and we assumed that $B$ is equal to 20 m/Myr,

based on the measured erosion rate of 21.1 m/Myr (TEN18-13) in the mainstem Nolichucky upstream of the knickzone (Table S5). We solved Eq. 6 to produce a steady-state profile as our initial condition. We then introduced a horizontal layer of more erodible rock at the outlet to represent incision into the sedimentary rocks of the Valley and Ridge. We varied the erodibility of this softer rock between 2 and 10 times the erodibility of the metamorphic rock.

After setting up the initial condition, we solved Eq. 5 using a forward-time, upwind-space finite-difference method (*88, 89*). When the rock contact reached the position where it is located today, we used the simulation to perform a synthetic calculation equivalent to our methodology described above. That is, we estimated the total amount of rock needed to be added back to the profile for the entire simulated Nolichucky River to be located in metamorphic rock. We compared this estimate to the actual time it took for the contact to migrate to its position in the numerical simulation. The estimated time in the synthetic calculation yields a comparatively older age than the actual time in the numerical simulation, but only by several thousand years, a difference of less than 1% (Fig. S12).

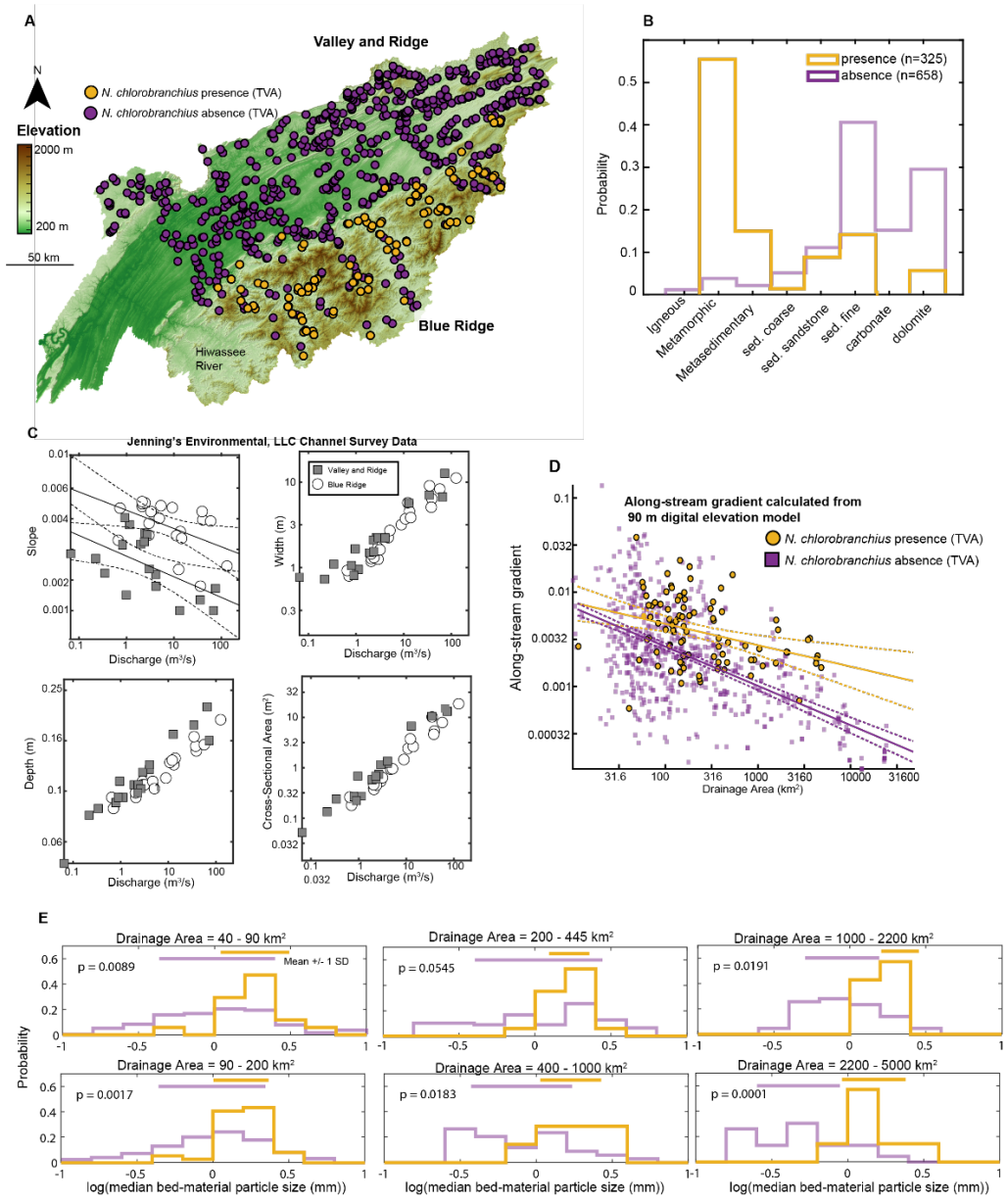


**Fig. S1. River channel characteristics in the Blue Ridge and Valley and Ridge.** (**A**) Topographic map of the upper Tennessee River basin with Tennessee Valley Authority (TVA) presence and absence data for *N. chlorobranchius.* Only data upstream of the Hiwassee River is included in the analysis. (**B**) Frequency of different rock types underlying 7-km stream reaches where *N. chlorobranchius* is present or absent. (**C**) Relationships between channel slope, width, depth, cross-sectional area and water discharge for Blue Ridge and Valley and Ridge rivers. (**D**) Relationship between channel slope measured from a DEM and drainage area for *N. chlorobranchius* presence and absence localities. (**E**) Histograms of predicted median bed-sediment particle size. The shaded lines above the bins represent the mean $\pm$ 1$\sigma$ and the p-value for a two-tailed t-test of the difference between means is reported.

**Table S1. ANCOVA Results for Channel Slope**

| | df | SS | MS | F |
|---|---|---|---|---|
| Groups | 1 | 5.28 | 5.28 | 38.03* |
| Discharge | 1 | 1.97 | 1.97 | 14.21* |
| Error | 36 | 5 | 0.14 | |

*Note: Homogeneity of regression tested and not significant: F = 0.05, p=0.83. Regression coefficient with $log_{10}$(Discharge) = -0.32*. The unadjusted and adjusted mean slope values for the groups (Blue Ridge and Valley and Ridge) are reported in Table S4.*
**The results of the F-Test are significant (p < 0.05).*

**Table S2. ANCOVA Results for Mean Bankfull Depth**

| | df | SS | MS | F |
|---|---|---|---|---|
| Groups | 1 | 0.32 | 0.32 | 19.64* |
| Discharge | 1 | 14.28 | 14.28 | 874* |
| Error | 36 | 0.57 | 0.016 | |

*Note: Homogeneity of regression tested and not significant: F = 0.6, p=0.45. Regression coefficient with $log_{10}$(Discharge) = 0.87*.*
**The results of the F-Test are significant (p < 0.05).*

**Table S3. ANCOVA Results for Channel Cross-Sectional Area**

| | df | SS | MS | F |
|---|---|---|---|---|
| Groups | 1 | 0.11 | 0.11 | 13.8* |
| Discharge | 1 | 3.03 | 3.03 | 384.5* |
| Error | 36 | 0.28 | 0.008 | |

*Note: Homogeneity of regression tested and not significant: F = 3.11, p=0.09. Regression coefficient with $log_{10}$(Discharge) = 0.40*.*
**The results of the F-Test are significant (p < 0.05).*

**Table S4. Unadjusted and adjusted means of channel cross-sectional geometry using water discharge as a covariate.**

| | | Unadjusted | | Adjusted | |
|---|---|---|---|---|---|
| Log10(Measurement) | Location | Mean | SE | Mean | SE |
| Channel Slope (m/m) | Blue Ridge | -1.61 | 0.35 | -1.49 | 0.25 |
| | Valley and Ridge | -2.25 | 0.53 | -2.27 | 0.25 |
| Mean Bankfull Depth (m) | Blue Ridge | 0.63 | 0.12 | 0.29 | 0.08 |
| | Valley and Ridge | 0.43 | 0.17 | 0.48 | 0.09 |
| Cross-Sectional Area ($m^2$) | Blue Ridge | -0.31 | 0.05 | -0.47 | 0.06 |
| | Valley and Ridge | -0.38 | 0.09 | -0.36 | 0.06 |

*Note: Adjusted means calculated at $log_{10}$(Discharge) = 0.46. There are 21 Blue Ridge data points and 18 in the Valley and Ridge. All data are log (base 10)-transformed.*

398

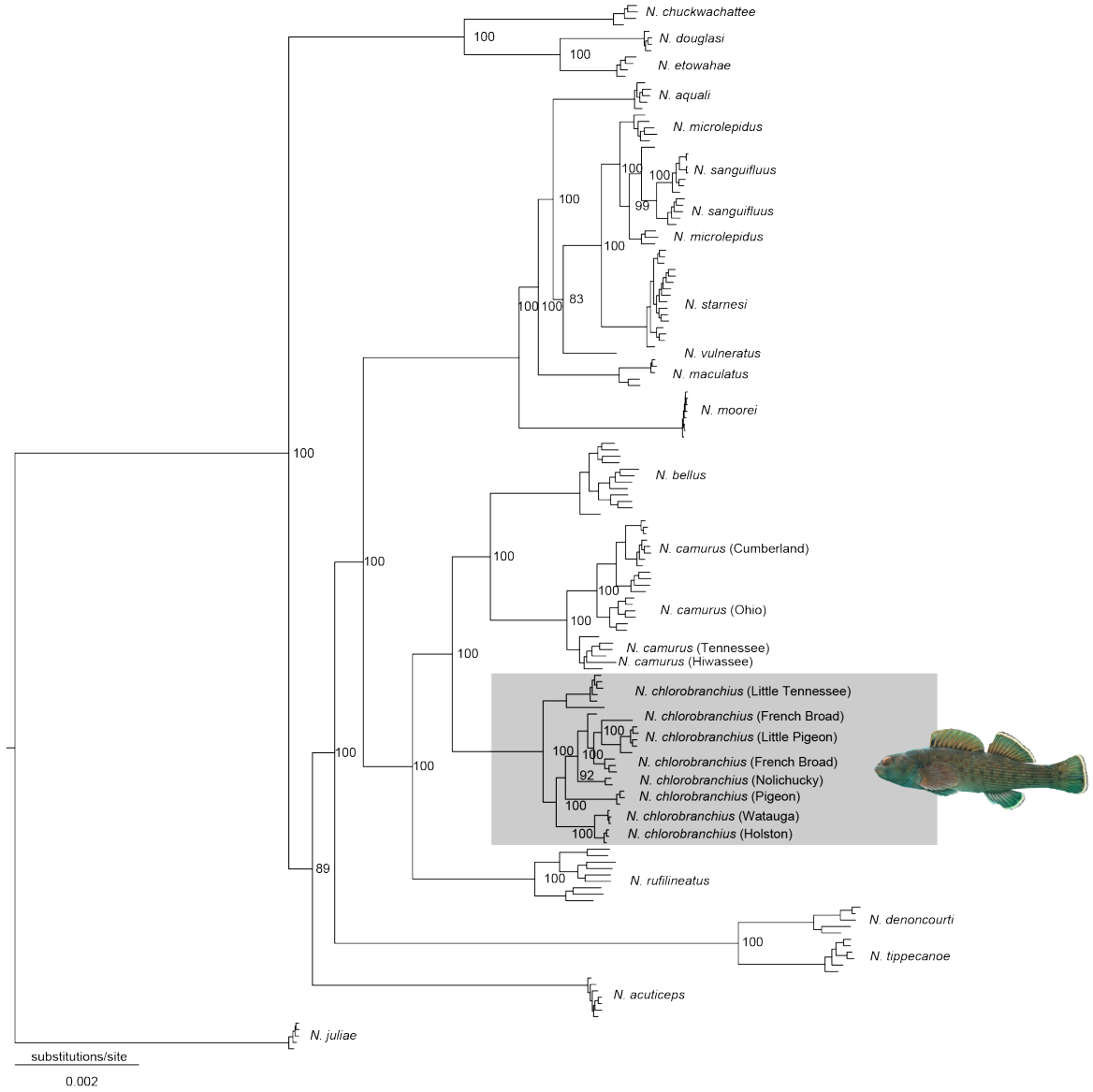


**Fig. S2. Phylogeny of *Nothonotus* inferred from concatenated ddRAD sequence data.** Numbers at nodes are bootstrap support values. The lineages comprising the *Nothonotus chlorobranchius* species complex is highlighted in the gray box. The photograph shows a *N. chlorobranchius* specimen from the Little Tennessee River (YPM_ICH 021891).

399

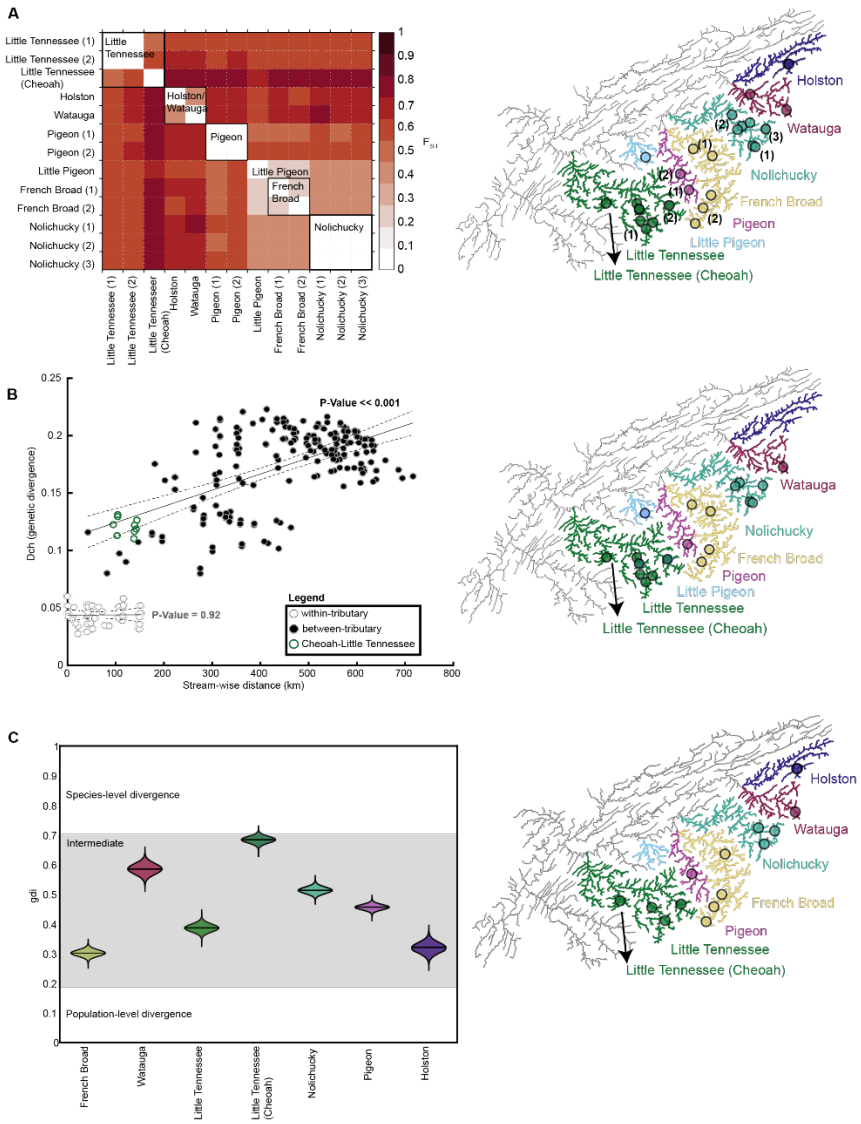


**Fig. S3. Additional metrics of genetic divergence.** The map to the right of each panel shows the localities represented in each analysis. (**A**) The fixation index ($F_{ST}$) between specimens split into groups as shown in the map. Within-tributary comparisons (outlined in black boxes) have smaller $F_{ST}$ values than between-tributary comparisons ($p < 0.001$, see main text). (**B**) Genetic divergence ($D_{CH}$) versus streamwise distance for within-tributary comparisons (white points) and between-tributary comparisons (black points). Points comparing the Cheoah River with other Little Tennessee localities are outlined in green. Least-squares linear regressions between genetic divergence and streamwise distance are shown for the within- and between-tributary comparisons. Dashed lines show the 95% confidence intervals. P-Values for an F-Test of the linear fit versus a constant model are reported next to the regressions. (**C**) Values of the genealogical divergence index (*gdi*) for the seven lineages in the ddRAD sequence phylogeny. The gray bar indicates intermediate *gdi* values consistent with either species-level or population-level divergence.

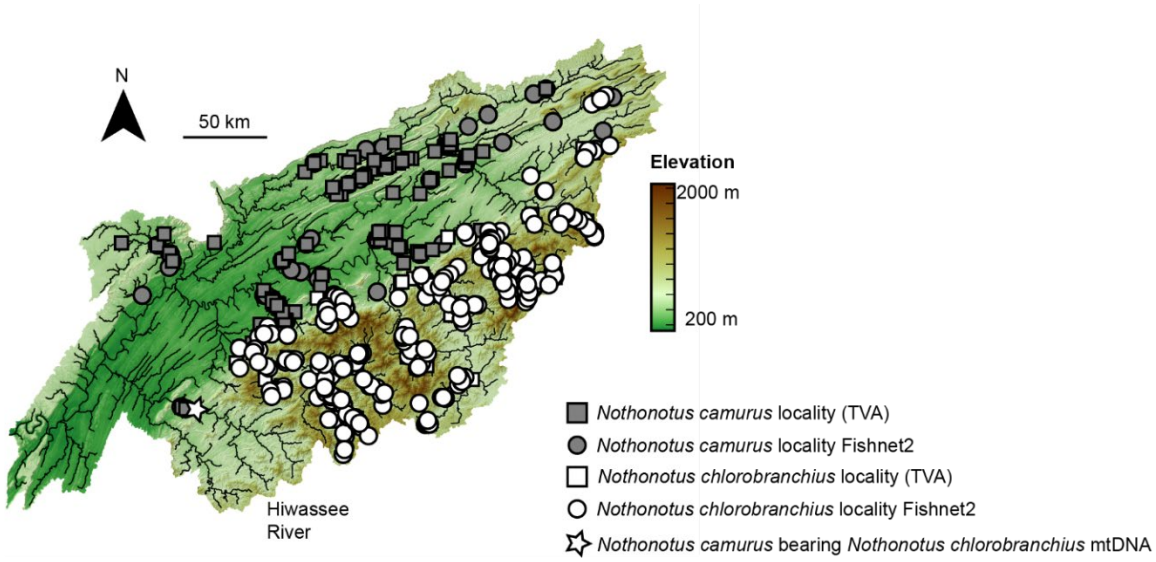


**Fig. S4. Locality data for *Nothonotus camurus* and *N. chlorobranchius*.** Locality data are from the Tennessee Valley Authority (TVA) collection records and from www.fishnet2.com, a database of vouchered museum specimens. The star represents the locality of a *N. camurus* specimen bearing a *N. chlorobranchius*-like mitochondrial genome indicating past hybridization.

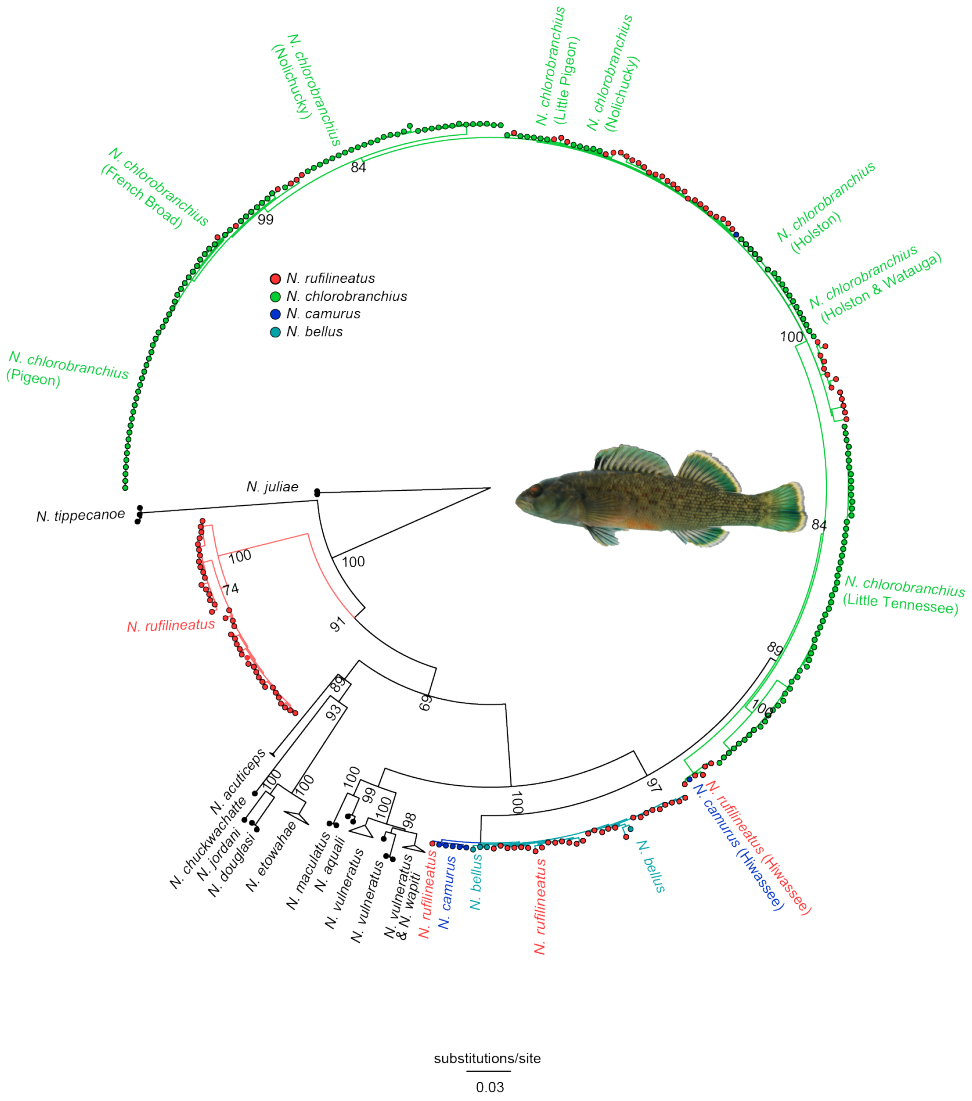


**Fig. S5. Phylogeny inferred from mtDNA gene *cytb* for all *Nothonotus*.** *Nothonotus rufilineatus* (red) shares haplotypes with *N. bellus* (teal), *N. camurus* (blue), and *N. chlorobranchius* (green). Although no *N. chlorobranchius* individuals were collected from the Hiwassee River, *N. rufilineatus* and *N. camurus* collected from the Hiwassee River share haplotypes that resolve as sister to all *N. chlorobranchius* in the mtDNA gene tree. We thus interpret this mtDNA haplotype as a mitochondrial fossil that contains information about an ancient population of *N. chlorobranchius* that hybridized with both *N. camurus* and *N. rufilineatus* and has since been extirpated or is rare. Numbers at nodes are bootstrap support values. The photograph shows a *N. chlorobranchius* specimen from the Nolichucky River (YPM_ICH 021990).

**A**

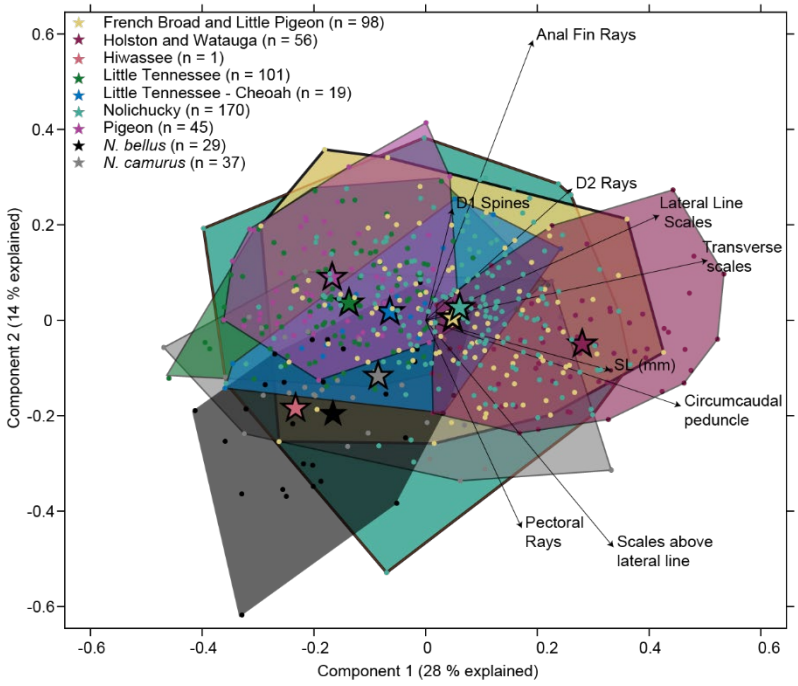


**B**

**Percentage of specimens correctly identified through a linear discriminant analysis**

| French Broad & Little Pigeon | Holston & Watauga | Little Tennessee | Little Tennessee (Cheoah) | Nolichucky | Pigeon | *N. bellus* | *N. camurus* |
|---|---|---|---|---|---|---|---|
| 31% | 80% | 49% | 42% | 46% | 53% | 93% | 41% |

**Fig. S6. Analysis of morphological traits of *Nothonotus chlorobranchius, Nothonotus bellus,* and *Nothonotus camurus*.** (**A**) Principal component analysis on nine morphological traits (black lines with arrows). Each specimen is plotted with a small dot and colored by the tributary from which it was collected. The centroid of the space each population occupies is plotted with a star, and the minimum bounding perimeter for specimens collected from each tributary is outlined and shaded. The pink star represents the one Hiwassee specimen sequenced in our study. (**B**) Percentage of specimens correctly identified in each group through a linear discriminant analysis.

401

402

403

404

405

406

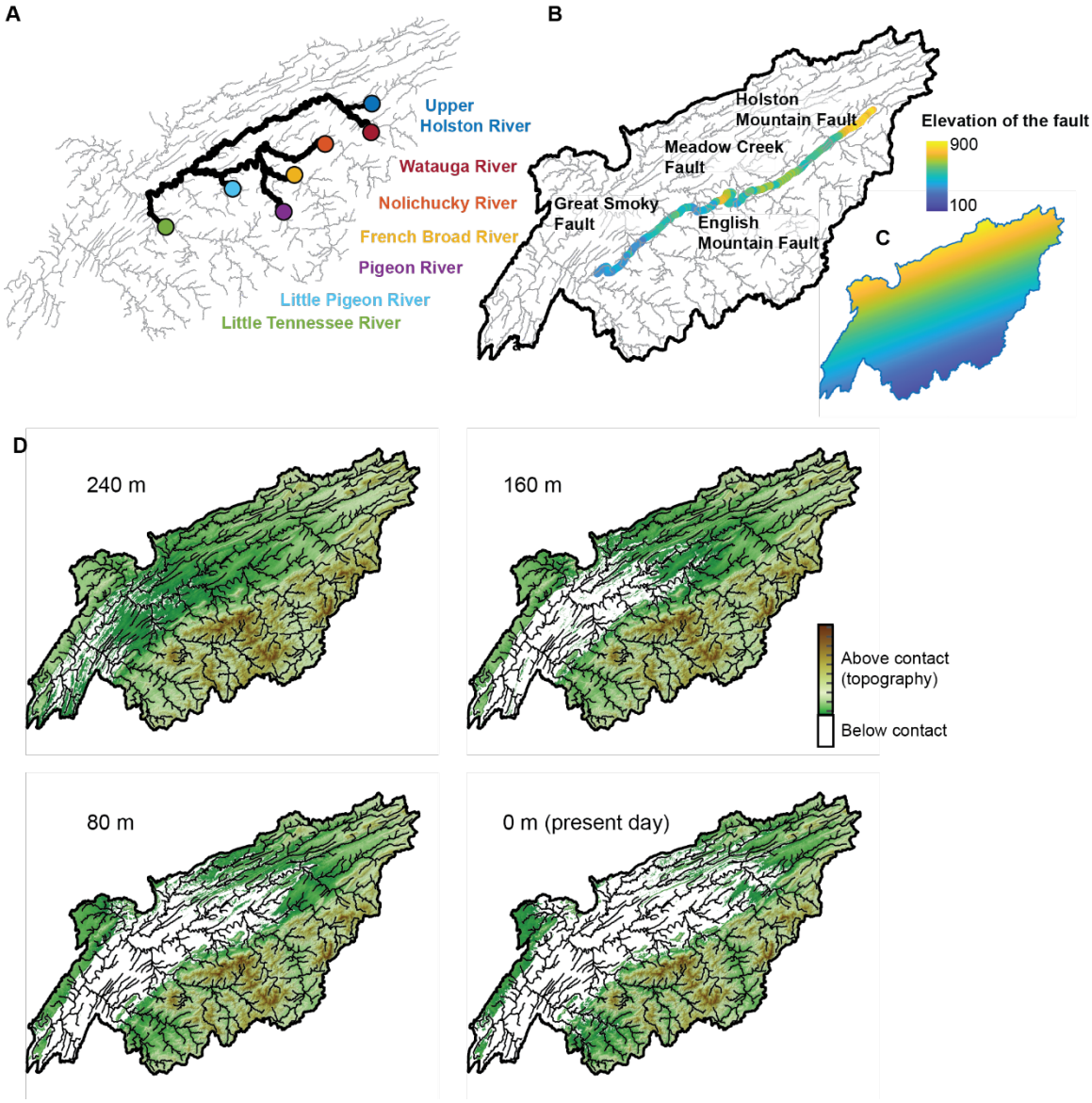


**Fig. S7. Visualization of a model for the exhumation of the metamorphic rocks of the Blue Ridge.** (**A**) The most downstream instance of *Nothonotus chlorobranchius* recorded in each of the tributaries (circles) and the pathways between them (black). We require that the entire pathway between any two points be located in metamorphic rock when constructing hypothetical phylogenies. (**B**) Location and elevation of the thrust faults separating the Blue Ridge and Valley and Ridge. (**C**) An example of a dipping plane that we use to represent the structure of the Blue Ridge Thrust Fault. Elevations in (**B**) and (**C**) are relative to mean sea level. (**D**) An example of the calculation for determining which parts of the landscape have eroded through the metamorphic rocks of the Blue Ridge and into the sedimentary rocks of the Valley and Ridge. Areas where sedimentary rock is predicted to be exposed are highlighted in white. The panels show the progression of isolation through erosion from when the landscape was 240 m above what it is today to the present for a fault dipping 6° degrees east of south and 0.02° below horizontal A similar illustration is shown in Fig. 3 in the main text.

407

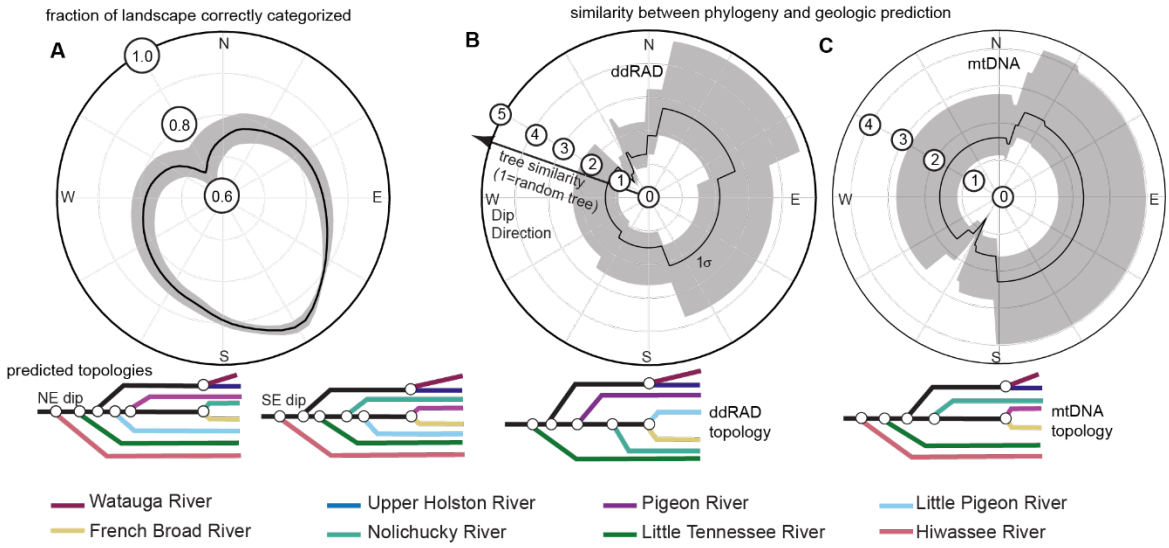


**Fig. S8. Comparison of genetic phylogenies to geologic evolutionary scenarios.** Results shown are analogous to Fig. 4 in the main text, but the analysis here excludes the Little Pigeon (ddRAD and mtDNA dendrograms) and the Pigeon (mtDNA dendrogram). Specimens from these tributaries are not resolved as monophyletic in the phylogenies. (**A**) The fraction of the landscape for which a geologic contact with a given dip direction correctly predicts the rock type (metamorphic or sedimentary) exposed at the surface. Dendrograms below are evolutionary scenarios predicted by the model of erosion into a geologic contact dipping to the NE or SE. (**B**) and **(C**) show the mutual clustering information between dendrograms representing the topologic relationships of lineages inferred from (**B**) the ddRAD phylogeny and (**C**) the mtDNA phylogeny and dendrograms predicted by erosion into a geologic contact dipping in a given direction at $1^{\circ}$ below horizontal, normalized by similarity to 1000 randomly generated dendrograms (Materials and Methods). Dashed lines in the dendrograms in (**B**) and (**C**) indicate tributaries where specimens were not resolved as monophyletic. In all polar plots the black line represents the mean and the shaded area represents $\pm$ 1σ.

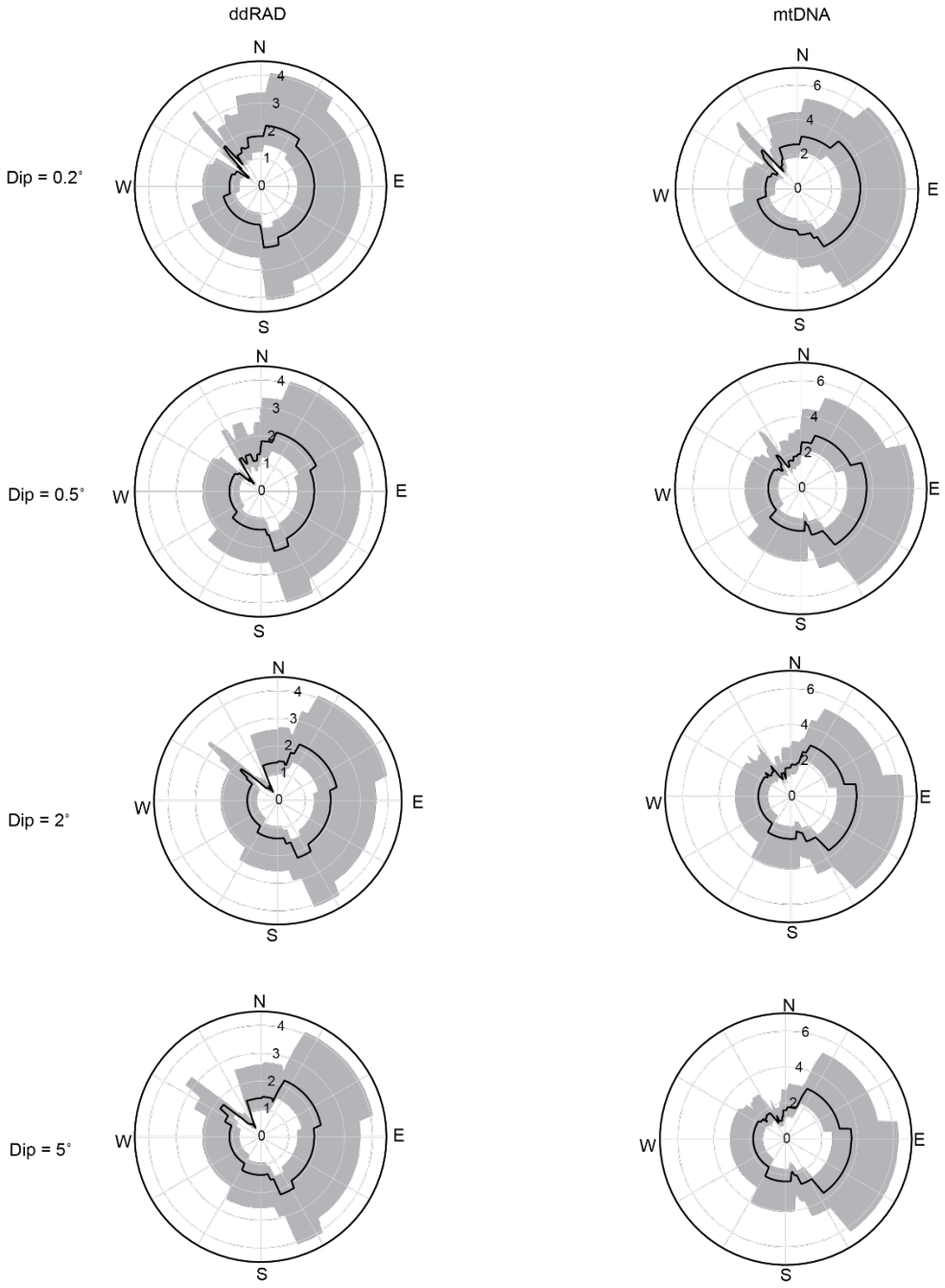


**Fig. S9. Comparison of genetic phylogenies to geologic evolutionary scenarios for different dip angles.** Results shown are analogous to Fig. 4 in the main text, but for different values of the dip angle below horizontal. The results in the main-text are for a dip angle of 1° below horizontal. The polar plots show the mutual clustering information between dendrograms representing the topologic relationships of lineages inferred from the ddRAD phylogeny (left panel) and the mtDNA phylogeny (right panel) and dendrograms predicted by erosion into a geologic contact dipping in a given direction for different dip angles (rows), normalized by similarity to 1000 randomly generated dendrograms. The black line represents the mean and the shaded area represents $\pm$ 1$\sigma$.

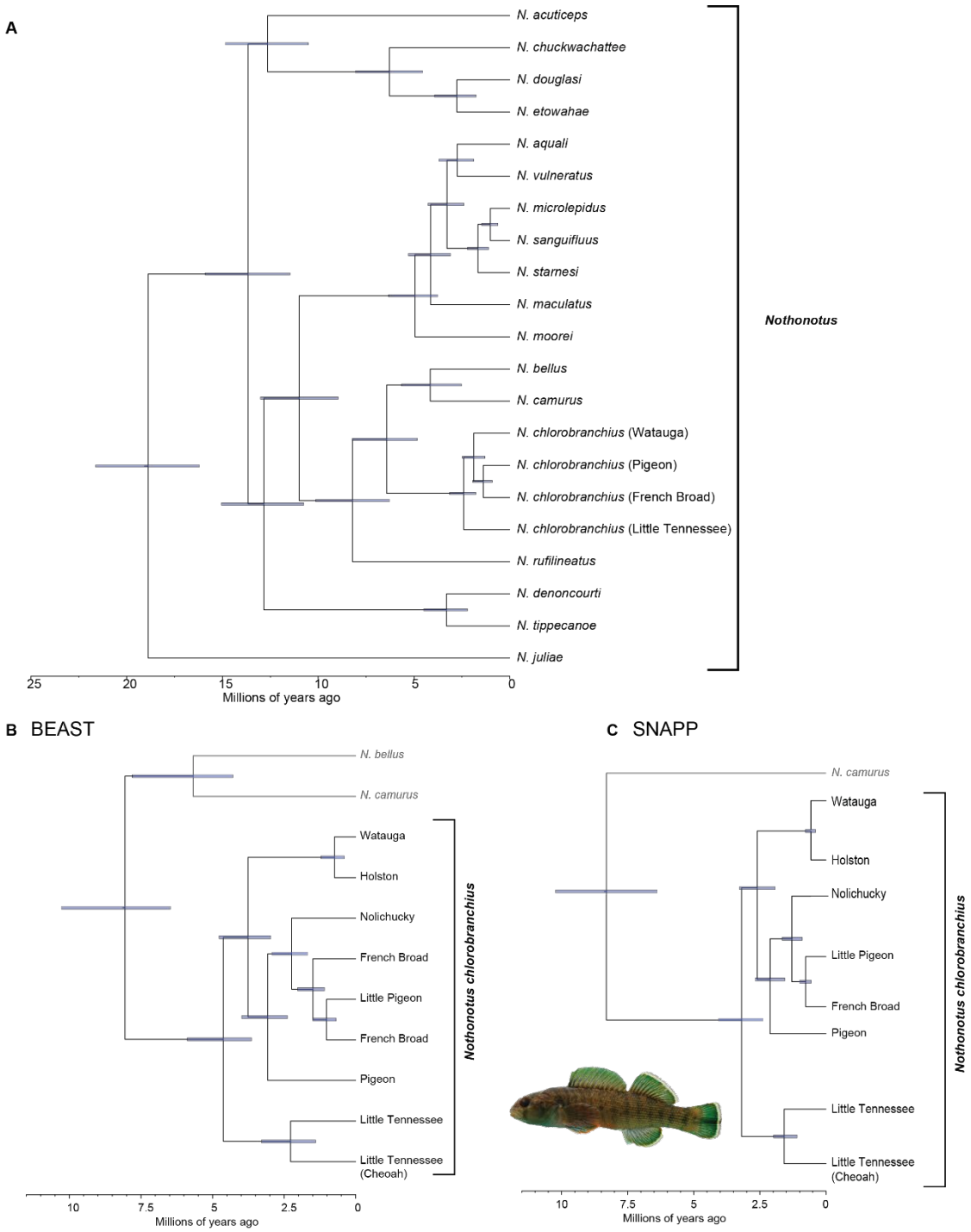


**Fig. S10. Time-calibrated phylogenies.** (**A**) Time-tree for *Nothonotus* inferred from concatenated ddRAD sequence data and used to calibrate the rate of molecular evolution that is in turn used to estimate the time-calibrated phylogeny of *N. chlorobranchius* (**B** and **C**) derived from a dataset of concatenated loci in BEAST (**B**) and from a multi-species coalescent model applied using SNAPP (**C**). The blue bars represent the 95% HPD estimate for the age of the node. The photograph shows a *N. chlorobranchius* specimen from the Pigeon River (YPM_ICH 021729).

417

418

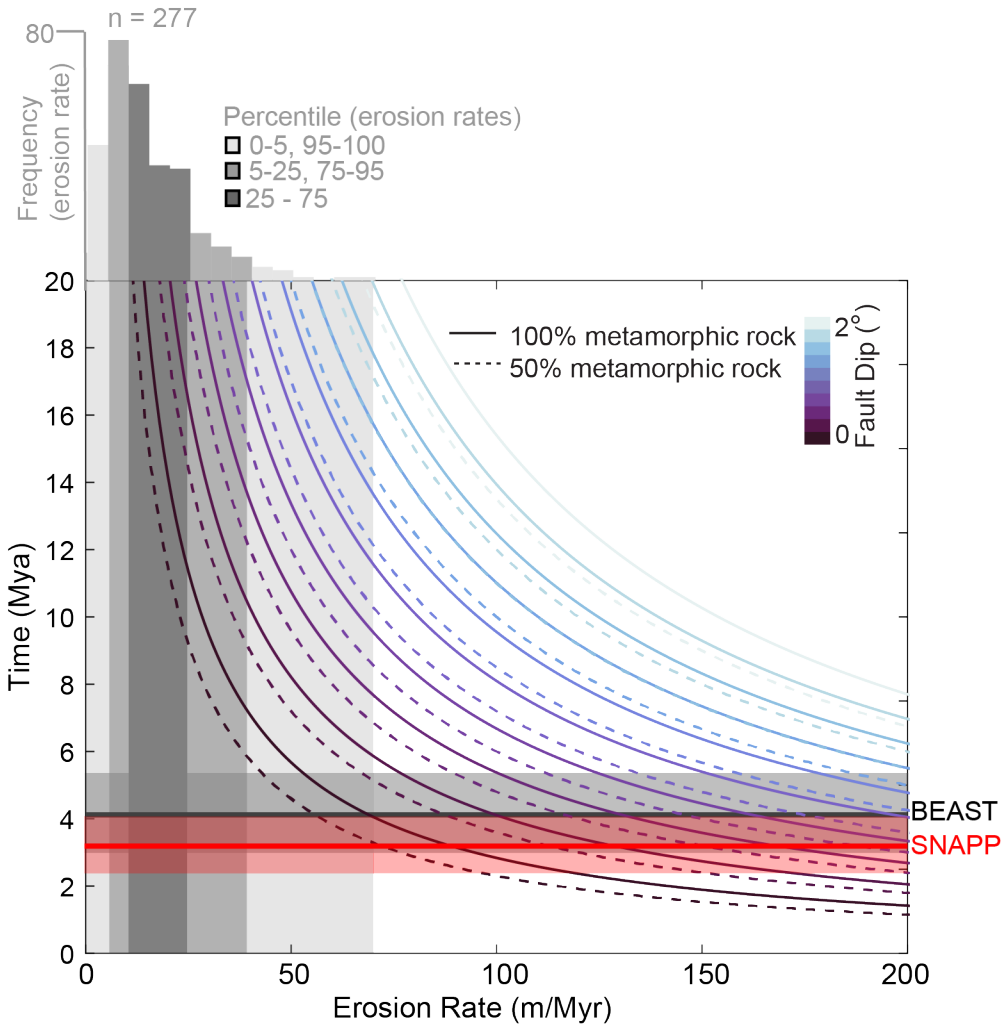


**Fig. S11. Comparison of absolute timing of divergence inferred from geologic and molecular datasets.** The estimated timing of isolation, in millions of years ago (Mya), between the Little Tennessee and Holston/Watauga clades as a function of fault dip and erosion rate. The lines are colored by the fault dip angle. Solid lines assume that the populations were connected when the pathways between tributaries were located in 100% metamorphic rock. Dashed lines only require that 50% of the pathway flows over metamorphic rock. A histogram of measured erosion rates from across the region is shown on top of the main plot. The bars are colored in shades of grey, representing percentile intervals. The horizontal lines represent the mean inferred ages since divergence from the most recent common ancestor of all *Nothonotus chlorobranchius* and the horizontal bars indicate the 95% highest posterior density (HPD) region of confidence. The grey horizontal line and bar represent the age derived from an analysis of concatenated loci in BEAST (Fig. S10B). The red line and bar represent the age estimate derived from a multi-coalescent analysis in SNAPP (Fig. S10C).

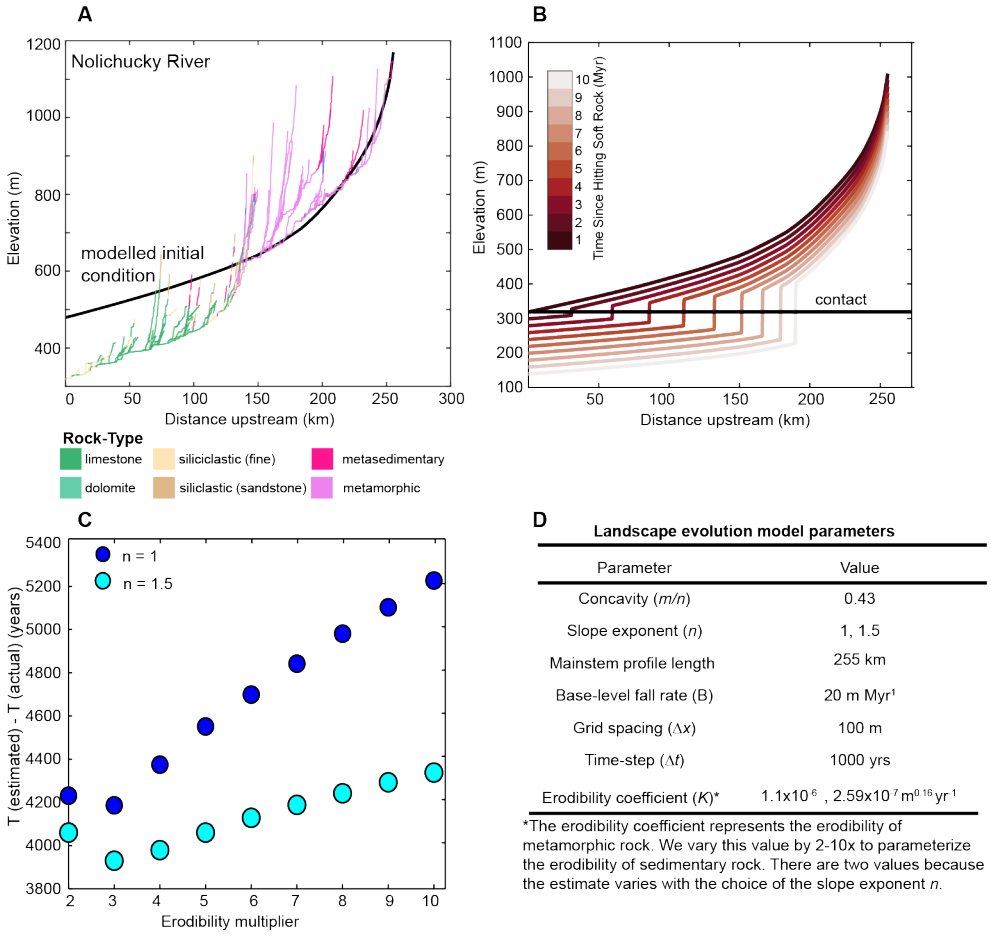


**Fig. S12. Synthetic test of geologic calculation for absolute timing of isolation.** (**A**) The modeled initial condition (black) and the actual present-day longitudinal profile of the Nolichucky River colored by the rock type it overlies. (**B**) The topographic evolution of the simulated Nolichucky River profile over time as it erodes into a layer of softer rock. The horizontal black line represents the initial elevation of the contact between sedimentary and metamorphic rock. (**C**) A comparison of a synthetic calculation analogous to the one we use in this study to the actual timing of isolation measured from the simulation. We perform this synthetic calculation for two values of $n$ and for sedimentary rock that is 2 to 10 times more erodible than the metamorphic rock. (**D**) Parameters used in the landscape evolution model.

| Sample ID | River | Longitude | Latitude | Drainage area ($km^2$) | $^{10}$Be concentration (atoms/g) | $^{10}$Be uncertainty (1σ, atoms/g) | Erosion rate (m/Myr) | 1σ Erosion rate uncertainty (m/Myr) |
|---|---|---|---|---|---|---|---|---|
| TEN18-01 | Betty Creek | 34.97668 | -83.43471 | 32.3 | 459400 | 9900 | 15.8 | 1.32 |
| TEN18-02 | Ledford Branch | 35.15237 | -83.25957 | 2.8 | 327800 | 9300 | 18.5 | 1.58 |
| TEN18-03 | Walnut Creek | 35.13922 | -83.27246 | 15.6 | 302700 | 6500 | 21.4 | 1.78 |
| TEN18-04 | Cullasaja River | 35.12205 | -83.28171 | 121.7 | 368900 | 10500 | 15.2 | 1.31 |
| TEN18-05 | Big Creek | 35.08174 | -83.20662 | 11.1 | 427300 | 8500 | 15 | 1.25 |
| TEN18-06 | Catheys Creek | 35.21316 | -82.78721 | 21.5 | 385500 | 7800 | 14.8 | 1.23 |
| TEN18-07 | Kuykendall Creek | 35.21390 | -82.78528 | 7.5 | 451800 | 10800 | 10.7 | 0.911 |
| TEN18-08 | Rice Creek | 36.01004 | -82.56195 | 15.5 | 291300 | 9000 | 18.4 | 1.58 |
| TEN18-09 | Rocky Fork | 36.04808 | -82.56071 | 22.2 | 415200 | 10700 | 18.1 | 1.53 |
| TEN18-10 | Jones Branch | 36.09970 | -82.43103 | 5.9 | 271800 | 8000 | 22.2 | 1.9 |
| TEN18-11 | Nolichucky River | 36.10135 | -82.44807 | 1644.1 | 242100 | 8300 | 43.2 | 3.74 |
| TEN18-12 | Hollow Poplar Creek | 36.08955 | -82.33287 | 12.6 | 486900 | 10700 | 11.2 | 0.941 |
| TEN18-13 | North Toe River | 36.04043 | -82.30597 | 1134.0 | 273700 | 7400 | 21.1 | 1.78 |
| TEN18-14 | Hurricane Creek | 35.72093 | -83.02543 | 22.1 | 296400 | 8200 | 18.4 | 1.57 |
| TEN18-15 | Pigeon River | 35.52446 | -82.84420 | 335.7 | 325900 | 16400 | 14.4 | 1.38 |
| TEN18-16 | Spring Creek | 35.87727 | -82.83523 | 182.2 | 276500 | 6100 | 16.7 | 1.4 |
| TEN18-17 | Paint Creek | 35.94735 | -82.89468 | 63.8 | 457000 | 10800 | 9.06 | 0.772 |
| TEN18-18 | Flat Creek | 35.73142 | -82.59518 | 41.6 | 510600 | 12500 | 9.94 | 0.847 |
| TEN18-19 | Worse Creek | 34.74100 | -83.35861 | 1.4 | 381500 | 7900 | 8.97 | 0.758 |
| TEN18-20 | Unnamed | 34.74333 | -83.35871 | 0.1 | 91400 | 3000 | 40.8 | 3.52 |
| TEN18-21 | Unnamed | 34.74742 | -83.37509 | 0.6 | 415800 | 9600 | 9.3 | 0.79 |

**Table S5. Cosmogenic-nuclide derived erosion rates and sample data for the Tennessee and Chattooga Rivers.**

| Sample name | Latitude | Longitude | Effective Elevation/Pressure (hPa) | Flag | Sample thickness (m) | Sample Density (g cm$^{-3}$) | Shield-ding | Erosion Rate (cm yr$^{-1}$) | Year | Nuclide | Min-eral | Concentra-tion (atoms g$^{-1}$) | 1σ Uncertainty (atoms g$^{-1}$) | Standardization |
|---|---|---|---|---|---|---|---|---|---|---|---|---|---|---|
| TN18-01 | 34.97668 | -83.4347 | 852.6973 | pre | 0 | 2.65 | 1 | 0 | 2018; | Be-10 | quartz | 459400 | 9900 | 07KNSTD; |
| TN18-02 | 35.15237 | -83.2596 | 882.5332 | pre | 0 | 2.65 | 1 | 0 | 2018; | Be-10 | quartz | 327800 | 9300 | 07KNSTD; |
| TN18-03 | 35.13922 | -83.2725 | 872.6323 | pre | 0 | 2.65 | 1 | 0 | 2018; | Be-10 | quartz | 302700 | 6500 | 07KNSTD; |
| TN18-04 | 35.12205 | -83.2817 | 892.6063 | pre | 0 | 2.65 | 1 | 0 | 2018; | Be-10 | quartz | 368900 | 10500 | 07KNSTD; |
| TN18-05 | 35.08175 | -83.2066 | 872.1197 | pre | 0 | 2.65 | 1 | 0 | 2018; | Be-10 | quartz | 427300 | 8500 | 07KNSTD; |
| TN18-06 | 35.21317 | -82.7872 | 890.7757 | pre | 0 | 2.65 | 1 | 0 | 2018; | Be-10 | quartz | 385500 | 7800 | 07KNSTD; |
| TN18-07 | 35.21391 | -82.7853 | 913.1273 | pre | 0 | 2.65 | 1 | 0 | 2018; | Be-10 | quartz | 451800 | 10800 | 07KNSTD; |
| TN18-08 | 36.01004 | -82.562 | 904.3202 | pre | 0 | 2.65 | 1 | 0 | 2018; | Be-10 | quartz | 291300 | 9000 | 07KNSTD; |
| TN18-09 | 36.04809 | -82.5607 | 851.34 | pre | 0 | 2.65 | 1 | 0 | 2018; | Be-10 | quartz | 415200 | 10700 | 07KNSTD; |
| TN18-10 | 36.09971 | -82.431 | 886.7063 | pre | 0 | 2.65 | 1 | 0 | 2018; | Be-10 | quartz | 271800 | 8000 | 07KNSTD; |
| TN18-11 | 36.10135 | -82.4481 | 804.8193 | pre | 0 | 2.65 | 1 | 0 | 2018; | Be-10 | quartz | 242100 | 8300 | 07KNSTD; |
| TN18-12 | 36.08955 | -82.3329 | 898.0353 | pre | 0 | 2.65 | 1 | 0 | 2018; | Be-10 | quartz | 486900 | 10700 | 07KNSTD; |
| TN18-13 | 36.04044 | -82.306 | 893.4386 | pre | 0 | 2.65 | 1 | 0 | 2018; | Be-10 | quartz | 273700 | 7400 | 07KNSTD; |
| TN18-14 | 35.72094 | -83.0254 | 900.4893 | pre | 0 | 2.65 | 1 | 0 | 2018; | Be-10 | quartz | 296400 | 8200 | 07KNSTD; |
| TN18-15 | 35.52446 | -82.8442 | 921.6295 | pre | 0 | 2.65 | 1 | 0 | 2018; | Be-10 | quartz | 325900 | 16400 | 07KNSTD; |
| TN18-16 | 35.87727 | -82.8352 | 926.2477 | pre | 0 | 2.65 | 1 | 0 | 2018; | Be-10 | quartz | 276500 | 6100 | 07KNSTD; |
| TN18-17 | 35.94736 | -82.8947 | 938.0244 | pre | 0 | 2.65 | 1 | 0 | 2018; | Be-10 | quartz | 457000 | 10800 | 07KNSTD; |
| TN18-18 | 35.73142 | -82.5952 | 906.6597 | pre | 0 | 2.65 | 1 | 0 | 2018; | Be-10 | quartz | 510600 | 12500 | 07KNSTD; |
| TN18-19 | 34.74101 | -83.3586 | 965.0252 | pre | 0 | 2.65 | 1 | 0 | 2018; | Be-10 | quartz | 381500 | 7900 | 07KNSTD; |
| TN18-20 | 34.74334 | -83.3587 | 965.7346 | pre | 0 | 2.65 | 1 | 0 | 2018; | Be-10 | quartz | 91400 | 3000 | 07KNSTD; |
| TN18-21 | 34.74743 | -83.3751 | 946.1743 | pre | 0 | 2.65 | 1 | 0 | 2018; | Be-10 | quartz | 415800 | 9600 | 07KNSTD; |

**Table S6. Inputs to Balco *et al. (73)* erosion rate calculator.** Effective atmospheric pressures for each basin were calculated using LSDTopoTools (*74*).

**Captions for Data S1 – S4**

Data S1: Locality data for *Nothonotus chlorobranchius* collected by the Tennessee Valley Authority and curated from Fishnet2.

Data S2: All tissue samples used for DNA sequencing in this study including GenBank and NCBI accession numbers.

Data S3: Morphological measurements for *Nothonotus bellus*, *Nothonotus camurus,* and *Nothonotus chlorobranchius.*

Data S4: Cosmogenic nuclide-derived erosion rate compilation for the southern and central Appalachian Mountains.

‘

**References and Notes**


1. C. Hoorn, V. Mosbrugger, A. Mulch, A. Antonelli, Biodiversity from mountain building. *Nat. Geosci.* **6**, 154–154 (2013). doi:10.1038/ngeo1742

2. A. Antonelli, W. D. Kissling, S. G. A. Flantua, M. A. Bermúdez, A. Mulch, A. N. Muellner-Riehl, H. Kreft, H. P. Linder, C. Badgley, J. Fjeldså, S. A. Fritz, C. Rahbek, F. Herman, H. Hooghiemstra, C. Hoorn, Geological and climatic influences on mountain biodiversity. *Nat. Geosci.* **11**, 718–725 (2018). doi:10.1038/s41561-018-0236-z

3. C. Rahbek, M. K. Borregaard, R. K. Colwell, B. Dalsgaard, B. G. Holt, N. Morueta-Holme, D. Nogues-Bravo, R. J. Whittaker, J. Fjeldså, Humboldt's enigma: What causes global patterns of mountain biodiversity? *Science* **365**, 1108–1113 (2019). doi:10.1126/science.aax0149 Medline

4. C. Hoorn, F. P. Wesselingh, H. ter Steege, M. A. Bermudez, A. Mora, J. Sevink, I. Sanmartín, A. Sanchez-Meseguer, C. L. Anderson, J. P. Figueiredo, C. Jaramillo, D. Riff, F. R. Negri, H. Hooghiemstra, J. Lundberg, T. Stadler, T. Särkinen, A. Antonelli, Amazonia through time: Andean uplift, climate change, landscape evolution, and biodiversity. *Science* **330**, 927–931 (2010). doi:10.1126/science.1194585 Medline

5. W. N. Ding, R. H. Ree, R. A. Spicer, Y. W. Xing, Ancient orogenic and monsoon-driven assembly of the world's richest temperate alpine flora. *Science* **369**, 578–581 (2020). doi:10.1126/science.abb4484 Medline

6. J. T. Weir, M. Price, Andean uplift promotes lowland speciation through vicariance and dispersal in *Dendrocincla* woodcreepers. *Mol. Ecol.* **20**, 4550–4563 (2011). doi:10.1111/j.1365-294X.2011.05294.x Medline

7. D. Craw, P. Upton, C. P. Burridge, G. P. Wallis, J. M. Waters, Rapid biological speciation driven by tectonic evolution in New Zealand. *Nat. Geosci.* **9**, 140–144 (2015). doi:10.1038/ngeo2618

8. L. P. Lagomarsino, F. L. Condamine, A. Antonelli, A. Mulch, C. C. Davis, The abiotic and biotic drivers of rapid diversification in Andean bellflowers (Campanulaceae). *New Phytol.* **210**, 1430–1442 (2016). doi:10.1111/nph.13920 Medline

9. L. M. Boschman, F. L. Condamine, Mountain radiations are not only rapid and recent: Ancient diversification of South American frog and lizard families related to Paleogene Andean orogeny and Cenozoic climate variations. *Global Planet. Change* **208**, 103704 (2022). doi:10.1016/j.gloplacha.2021.103704

10. D. R. Montgomery, Coevolution of the Pacific salmon and Pacific Rim topography. *Geology* **28**, 1107–1110 (2000). doi:10.1130/0091-7613(2000)28<1107:COTPSA>2.0.CO;2

11. J. G. Lundberg, M. Kottelat, G. R. Smith, M. L. J. Stiassny, A. C. Gill, So many fishes, so little time: An overview of recent ichthyological discovery in continental waters. *Ann. Mo. Bot. Gard.* **87**, 26–62 (2000). doi:10.2307/2666207

12. D. Griffiths, Why does freshwater fish species richness differ between Pacific and Atlantic drainages of the Americas? *J. Biogeogr.* **45**, 784–792 (2018). doi:10.1111/jbi.13167

13. J. April, R. L. Mayden, R. H. Hanner, L. Bernatchez, Genetic calibration of species diversity among North America's freshwater fishes. *Proc. Natl. Acad. Sci. U.S.A.* **108**, 10602–10607 (2011). doi:10.1073/pnas.1016437108 Medline

14. G. R. Smith, C. Badgley, T. P. Eiting, P. S. Larson, Species diversity gradients in relation to geological history in North American freshwater fishes. *Evol. Ecol. Res.* **12**, 693–726 (2010).

15. B. M. Burr, L. M. Page, "Zoogeography of the fishes of the lower Ohio–upper Mississippi Basin" in *The Zoogeography of North American Freshwater Fishes*, C. H. Hocutt, E. O. Wiley, Eds. (Wiley, 1986).

16. R. L. Mayden, Vicariance biogeography, parsimony, and evolution in North American freshwater fishes. *Syst. Zool.* **37**, 329–355 (1988). doi:10.2307/2992197

17. C. M. Bossu, J. M. Beaulieu, P. A. Ceas, T. J. Near, Explicit tests of palaeodrainage connections of southeastern North America and the historical biogeography of Orangethroat Darters (Percidae: *Etheostoma*: *Ceasia*). *Mol. Ecol.* **22**, 5397–5417 (2013). doi:10.1111/mec.12485 Medline

18. K. H. Kozak, R. A. Blaine, A. Larson, Gene lineages and eastern North American palaeodrainage basins: Phylogeography and speciation in salamanders of the *Eurycea bislineata* species complex. *Mol. Ecol.* **15**, 191–207 (2006). doi:10.1111/j.1365-294X.2005.02757.x Medline

19. P. R. Hollingsworth Jr., T. J. Near, Temporal patterns of diversification and microendemism in Eastern Highland endemic barcheek darters (Percidae: Etheostomatinae). *Evolution* **63**, 228–243 (2009). doi:10.1111/j.1558-5646.2008.00531.x Medline

20. T. J. Near, B. P. Keck, Dispersal, vicariance, and timing of diversification in *Nothonotus* darters. *Mol. Ecol.* **14**, 3485–3496 (2005). doi:10.1111/j.1365-294X.2005.02671.x Medline

21. S. F. Gallen, Lithologic controls on landscape dynamics and aquatic species evolution in post-orogenic mountains. *Earth Planet. Sci. Lett.* **493**, 150–160 (2018). doi:10.1016/j.epsl.2018.04.029

22. M. Perne, M. D. Covington, E. A. Thaler, J. M. Myre, Steady state, erosional continuity, and the topography of landscapes developed in layered rocks. *Earth Surf. Dyn.* **5**, 85–100 (2017). doi:10.5194/esurf-5-85-2017

23. A. M. Forte, B. J. Yanites, K. X. Whipple, Complexities of landscape evolution during incision through layered stratigraphy with contrasts in rock strength. *Earth Surf. Process. Landf.* **41**, 1736–1757 (2016). doi:10.1002/esp.3947

24. Materials and methods are available as supplementary materials.

25. N. D. Jackson, B. C. Carstens, A. E. Morales, B. C. O'Meara, Species delimitation with gene flow. *Syst. Biol.* **66**, 799–812 (2017). Medline

26. S. A. S. Anderson, J. T. Weir, The role of divergent ecological adaptation during allopatric speciation in vertebrates. *Science* **378**, 1214–1218 (2022). doi:10.1126/science.abo7719 Medline

27. D. A. Etnier, W. C. Starnes, *The Fishes of Tennessee* (Univ. of Tennessee Press, 1993).

28. D. J. Eisenhour, Systematics of *Etheostoma camurum* and *E. chlorobranchium* (Osteichthyes, Percidae) in the Tennessee and Cumberland River drainages with analysis of hybridization in the Nolichucky River system. *Copeia* **1995**, 368–379 (1995). doi:10.2307/1446900

29. B. P. Keck, T. J. Near, Geographic and temporal aspects of mitochondrial replacement in *Nothonotus* darters (Teleostei: Percidae: Etheostomatinae). *Evolution* **64**, 1410–1428 (2010). Medline

30. T. J. Near, C. M. Bossu, G. S. Bradburd, R. L. Carlson, R. C. Harrington, P. R. Hollingsworth Jr., B. P. Keck, D. A. Etnier, Phylogeny and temporal diversification of darters (Percidae: Etheostomatinae). *Syst. Biol.* **60**, 565–595 (2011). doi:10.1093/sysbio/syr052 Medline

31. T. J. Near, B. P. Keck, Free from mitochondrial DNA: Nuclear genes and the inference of species trees among closely related darter lineages (Teleostei: Percidae: Etheostomatinae). *Mol. Phylogenet. Evol.* **66**, 868–876 (2013). doi:10.1016/j.ympev.2012.11.009 Medline

32. R. C. Harrington, J. W. Simmons, T. J. Near, The geographic distribution of the imperiled Barrens Darter, *Etheostoma forbesi*, and threats of hybridization with the closely related Fringed Darter, *Etheostoma crossopterum*. *Bull. Peabody Mus. Nat. Hist.* **61**, 3–21 (2020). doi:10.3374/014.061.0101

33. F. A. Cook, D. S. Albaugh, L. D. Brown, S. Kaufman, J. E. Oliver, R. D. Hatcher, Thin-skinned tectonics in the crystalline southern Appalachians; COCORP seismic-reflection profiling of the Blue Ridge and Piedmont. *Geology* **7**, 563–567 (1979). doi:10.1130/0091-7613(1979)7<563:TTITCS>2.0.CO;2

34. F. A. Cook, K. Vasudevan, Reprocessing and enhanced interpretation of the initial COCORP Southern Appalachians traverse. *Tectonophysics* **420**, 161–174 (2006). doi:10.1016/j.tecto.2006.01.022

35. R. D. Hatcher, P. J. Lemiszki, J. B. Whisner, Character of rigid boundaries and internal deformation of the southern Appalachian foreland fold-thrust belt. *Spec. Pap. Geol. Soc. Am.* **433**, 243–276 (2007). doi:10.1130/2007.2433(12)

36. P. Molnar, Late Cenozoic increase in accumulation rates of terrestrial sediment: How might climate change have affected erosion rates? *Annu. Rev. Earth Planet. Sci.* **32**, 67–89 (2004). doi:10.1146/annurev.earth.32.091003.143456

37. D. M. Anthony, D. E. Granger, A new chronology for the age of Appalachian erosional surfaces determined by cosmogenic nuclides in cave sediments. *Earth Surf. Process. Landf.* **32**, 874–887 (2007). doi:10.1002/esp.1446

38. J. M. Waters, D. Craw, C. P. Burridge, M. Kennedy, T. M. King, G. P. Wallis, Within-river genetic connectivity patterns reflect contrasting geomorphology. *J. Biogeogr.* **42**, 2452–2460 (2015). doi:10.1111/jbi.12608

39. J. M. Waters, B. C. Emerson, P. Arribas, G. A. McCulloch, Dispersal reduction: Causes, genomic mechanisms, and evolutionary consequences. *Trends Ecol. Evol.* **35**, 512–522 (2020). doi:10.1016/j.tree.2020.01.012 Medline

40. T. G. Farr, M. Kobrick, Shuttle radar topography mission produces a wealth of data. *Eos* **81**, 583–585 (2000). doi:10.1029/EO081i048p00583

41. W. Schwanghart, D. Scherler, TopoToolbox 2 – MATLAB-based software for topographic analysis and modeling in Earth surface sciences. *Earth Surf. Dyn.* **2**, 1–7 (2014). doi:10.5194/esurf-2-1-2014

42. J. D. Horton, C. A. San Juan, D. B. Stoeser, The State Geologic Map Compilation (SGMC) geodatabase of the conterminous United States (ver. 1.1, August 2017), US Geological Survey Data Series 1052 (2017); https://doi.org/10.3133/ds1052.

43. G. W. Abeshu, H.-Y. Li, Z. Zhu, Z. Tan, L. R. Leung, Median bed-material sediment particle size across rivers in the contiguous US. *Earth Syst. Sci. Data* **14**, 929–942 (2022). doi:10.5194/essd-14-929-2022

44. Jennings Environmental, LLC, "Tennessee Reference Stream Morphology and Large Woody Debris Assessment: Report and Guidebook" (Tennessee Department of Environment and Conservation, 2017).

45. B. P. Keck, T. J. Near, A young clade repeating an old pattern: diversity in *Nothonotus* darters (Teleostei: Percidae) endemic to the Cumberland River. *Mol. Ecol.* **19**, 5030–5042 (2010). doi:10.1111/j.1365-294X.2010.04866.x Medline

46. B. P. Keck, T. J. Near, Assessing phylogenetic resolution among mitochondrial, nuclear, and morphological datasets in *Nothonotus* darters (Teleostei: Percidae). *Mol. Phylogenet. Evol.* **46**, 708–720 (2008). doi:10.1016/j.ympev.2007.08.015 Medline

47. B. K. Peterson, J. N. Weber, E. H. Kay, H. S. Fisher, H. E. Hoekstra, Double digest RADseq: An inexpensive method for de novo SNP discovery and genotyping in model and non-model species. *PLOS ONE* **7**, e37135 (2012). doi:10.1371/journal.pone.0037135 Medline

48. D. Kim, B. H. Bauer, T. J. Near, Introgression and species delimitation in the Longear Sunfish *Lepomis megalotis* (Teleostei: Percomorpha: Centrarchidae). *Syst. Biol.* **71**, 273–285 (2022). doi:10.1093/sysbio/syab029 Medline

49. D. A. R. Eaton, I. Overcast, ipyrad: Interactive assembly and analysis of RADseq datasets. *Bioinformatics* **36**, 2592–2594 (2020). doi:10.1093/bioinformatics/btz966 Medline

50. E. McCartney-Melstad, M. Gidiş, H. B. Shaffer, An empirical pipeline for choosing the optimal clustering threshold in RADseq studies. *Mol. Ecol. Resour.* **19**, 1195–1204 (2019). doi:10.1111/1755-0998.13029 Medline

51. K. Katoh, D. M. Standley, MAFFT multiple sequence alignment software version 7: Improvements in performance and usability. *Mol. Biol. Evol.* **30**, 772–780 (2013). doi:10.1093/molbev/mst010 Medline

52. S. Kumar, G. Stecher, M. Li, C. Knyaz, K. Tamura, MEGA X: Molecular Evolutionary Genetics Analysis across computing platforms. *Mol. Biol. Evol.* **35**, 1547–1549 (2018). doi:10.1093/molbev/msy096 Medline

53. E. W. Sayers, R. Agarwala, E. E. Bolton, J. R. Brister, K. Canese, K. Clark, R. Connor, N. Fiorini, K. Funk, T. Hefferon, J. B. Holmes, S. Kim, A. Kimchi, P. A. Kitts, S. Lathrop, Z. Lu, T. L. Madden, A. Marchler-Bauer, L. Phan, V. A. Schneider, C. L. Schoch, K. D. Pruitt, J. Ostell, Database resources of the National Center for Biotechnology Information. *Nucleic Acids Res.* **47**, D23–D28 (2019). doi:10.1093/nar/gky1069 Medline

54. B. Q. Minh, H. A. Schmidt, O. Chernomor, D. Schrempf, M. D. Woodhams, A. von Haeseler, R. Lanfear, IQ-TREE 2: New models and efficient methods for phylogenetic inference in the genomic era. *Mol. Biol. Evol.* **37**, 1530–1534 (2020). doi:10.1093/molbev/msaa015 Medline

55. S. Kalyaanamoorthy, B. Q. Minh, T. K. F. Wong, A. von Haeseler, L. S. Jermiin, ModelFinder: Fast model selection for accurate phylogenetic estimates. *Nat. Methods* **14**, 587–589 (2017). doi:10.1038/nmeth.4285 Medline

56. D. T. Hoang, O. Chernomor, A. von Haeseler, B. Q. Minh, L. S. Vinh, UFBoot2: Improving the ultrafast bootstrap approximation. *Mol. Biol. Evol.* **35**, 518–522 (2018). doi:10.1093/molbev/msx281 Medline

57. R. Bouckaert, T. G. Vaughan, J. Barido-Sottani, S. Duchêne, M. Fourment, A. Gavryushkina, J. Heled, G. Jones, D. Kühnert, N. De Maio, M. Matschiner, F. K. Mendes, N. F. Müller, H. A. Ogilvie, L. du Plessis, A. Popinga, A. Rambaut, D. Rasmussen, I. Siveroni, M. A. Suchard, C.-H. Wu, D. Xie, C. Zhang, T. Stadler, A. J. Drummond, BEAST 2.5: An advanced software platform for Bayesian evolutionary analysis. *PLOS Comput. Biol.* **15**, e1006650 (2019). doi:10.1371/journal.pcbi.1006650 Medline

58. D. Bryant, R. Bouckaert, J. Felsenstein, N. A. Rosenberg, A. RoyChoudhury, Inferring species trees directly from biallelic genetic markers: Bypassing gene trees in a full coalescent analysis. *Mol. Biol. Evol.* **29**, 1917–1932 (2012). doi:10.1093/molbev/mss086 Medline

59. B. S. Weir, C. C. Cockerham, Estimating F-statistics for the analysis of population structure. *Evolution* **38**, 1358–1370 (1984). Medline

60. J. Goudet, HIERFSTAT, a package for R to compute and test hierarchical F-statistics. *Mol. Ecol. Notes* **5**, 184–186 (2005). doi:10.1111/j.1471-8286.2004.00828.x

61. B. Pfeifer, U. Wittelsbürger, S. E. Ramos-Onsins, M. J. Lercher, PopGenome: An efficient Swiss army knife for population genomic analyses in R. *Mol. Biol. Evol.* **31**, 1929–1936 (2014). doi:10.1093/molbev/msu136 Medline

62. M. Nei, *Molecular Evolutionary Genetics* (Columbia Univ. Press, 1987).

63. B. Rannala, Z. Yang, Efficient Bayesian species tree inference under the multispecies coalescent. *Syst. Biol.* **66**, 823–842 (2017). doi:10.1093/sysbio/syw119 Medline

64. W. Hamilton, "Geology of the Richardson Cove and Jones Cove quadrangles, Tennessee" (Professional Paper 349-A, US Geological Survey, 1961).

65. R.B. Neuman, "Geology of the Blockhouse quadrangle, Tennessee" (Geologic Quadrangle Map GQ-131, US Geological Survey, 1969).

66. R.B. Neuman, R.L. Wilson, "Geology of the Wildwood quadrangle, Tennessee" (Geologic Quadrangle Map GQ-130, US Geological Survey, 1969).

67. J. Rodgers, “Geologic map of east Tennessee with explanatory text” (Bulletin 58, Part II, Tennessee Division of Geology, 1953).

68. M. R. Smith, Information theoretic generalized Robinson-Foulds metrics for comparing phylogenetic trees. *Bioinformatics* **36**, 5007–5013 (2020). doi:10.1093/bioinformatics/btaa614 Medline

69. C. P. Kohl, K. Nishiizumi, Chemical isolation of quartz for measurement of *in-situ*-produced cosmogenic nuclides. *Geochim. Cosmochim. Acta* **56**, 3583–3587 (1992). doi:10.1016/0016-7037(92)90401-4

70. R. G. Ditchburn, N. E. Whitehead, “The separation of $^{10}$Be from silicates,” 3rd SPERA (South Pacific Environmental Radioactivity Association) Workshop, Canberra, Australia, 15 to 17 February 1994, pp. 4–7.

71. J. O. Stone, “Extraction of Al & Be from quartz for isotopic analysis” (2001); http://depts.washington.edu/cosmolab/chem/Al-26_Be-10.pdf.

72. K. Nishiizumi, M. Imamura, M. W. Caffee, J. R. Southon, R. C. Finkel, J. McAninch, Absolute calibration of $^{10}$Be AMS standards. *Nucl. Instrum. Methods Phys. Res. B* **258**, 403–413 (2007). doi:10.1016/j.nimb.2007.01.297

73. G. Balco, J. O. Stone, N. A. Lifton, T. J. Dunai, A complete and easily accessible means of calculating surface exposure ages or erosion rates from $^{10}$Be and $^{26}$Al measurements. *Quat. Geochronol.* **3**, 174–195 (2008). doi:10.1016/j.quageo.2007.12.001

74. S. M. Mudd, M.-A. Harel, M. D. Hurst, S. W. D. Grieve, S. M. Marrero, The CAIRN method: Automated, reproducible calculation of catchment-averaged denudation rates from cosmogenic nuclide concentrations. *Earth Surf. Dyn.* **4**, 655–674 (2016). doi:10.5194/esurf-4-655-2016

75. R. A. DiBiase, Increasing vertical attenuation length of cosmogenic nuclide production on steep slopes negates topographic shielding corrections for catchment erosion rates. *Earth Surf. Dyn.* **6**, 923–931 (2018). doi:10.5194/esurf-6-923-2018

76. J. O. Stone, Air pressure and cosmogenic isotope production. *J. Geophys. Res.* **105**, 23753–23759 (2000). doi:10.1029/2000JB900181

77. D. Lal, Cosmic ray labeling of erosion surfaces: In situ nuclide production rates and erosion models. *Earth Planet. Sci. Lett.* **104**, 424–439 (1991). doi:10.1016/0012-821X(91)90220-C

78. J. Duxbury, P. R. Bierman, E. W. Portenga, M. J. Pavich, S. Southworth, S. P. H. T. Freeman, Erosion rates in and around Shenandoah National Park, Virginia, determined using analysis of cosmogenic $^{10}$Be. *Am. J. Sci.* **315**, 46–76 (2015). doi:10.2475/01.2015.02

79. C. L. Linari, P. R. Bierman, E. W. Portenga, M. J. Pavich, R. C. Finkel, S. P. H. T. Freeman, Rates of erosion and landscape change along the Blue Ridge escarpment, southern Appalachian Mountains, estimated from *in situ* cosmogenic $^{10}$Be. *Earth Surf. Process. Landf.* **42**, 928–940 (2017). doi:10.1002/esp.4051

80. A. Matmon, P. R. Bierman, J. Larsen, S. Southworth, M. Pavich, M. Caffee, Temporally and spatially uniform rates of erosion in the southern Appalachian Great Smoky Mountains.

*Geology* **31**, 155–158 (2003). doi:10.1130/0091-7613(2003)031<0155:TASURO>2.0.CO;2

81. L. Reusser, P. Bierman, D. Rood, Quantifying human impacts on rates of erosion and sediment transport at a landscape scale. *Geology* **43**, 171–174 (2015). doi:10.1130/G36272.1

82. T. Marstellar, "Investigating sediment source to sink processes in a post-orogenic landscape," thesis, Georgia Institute of Technology (2012).

83. J. M. Reuter, "Erosion rates and patterns inferred from cosmogenic $^{10}$Be in the Susquehanna River Basin," thesis, University of Vermont (2005).

84. M. F. Stokes, I. J. Larsen, S. L. Goldberg, S. W. McCoy, P. P. Prince, J. T. Perron, The erosional signature of drainage divide motion along the Blue Ridge Escarpment. *J. Geophys. Res. Earth Surf.* **128**, e2022JF006757 (2023). doi:10.1029/2022JF006757

85. A. D. Howard, W. E. Dietrich, M. A. Seidl, Modeling fluvial erosion on regional to continental scales. *J. Geophys. Res.* **99**, 13971–13986 (1994). doi:10.1029/94JB00744

86. J. T. Perron, L. Royden, An integral approach to bedrock river profile analysis. *Earth Surf. Process. Landf.* **38**, 570–576 (2013). doi:10.1002/esp.3302

87. C. Wobus, K. X. Whipple, E. Kirby, N. Snyder, J. Johnson, K. Spyropolou, B. Crosby, D. Sheehan Tectonics from topography: Procedures, promise, and pitfalls. *Spec. Pap. Geol. Soc. Am.* **398**, 55–74 (2006).

88. J. T. Perron, W. E. Dietrich, J. W. Kirchner, Controls on the spacing of first-order valleys. *J. Geophys. Res.* **113**, F04016 (2008). doi:10.1029/2007JF000977

89. J. T. Perron, J. W. Kirchner, W. E. Dietrich, Formation of evenly spaced ridges and valleys. *Nature* **460**, 502–505 (2009). doi:10.1038/nature08174